CHEMISTRY
A EUROPEAN JOURNAL

DOI: 10.1002/chem.200600711

Hydrogen-Atom Transfer in Open-Shell Organometallic Chemistry: The Reactivity of Rh^{II}(cod) and Ir^{II}(cod) Radicals

Dennis G. H. Hetterscheid,[a] Martijn Klop,[a] Reinout J. N. A. M. Kicken,[a] Jan M. M. Smits,[a] Eduard J. Reijerse,[b] and Bas de Bruin*[c]

Abstract: A series of new metalloradical rhodium and iridium complexes $[M^{II}(cod)(N\text{-ligand})]^{2+}$ in the uncommon oxidation state +II were synthesized by one-electron oxidation of their $[M^{I}(cod)(N\text{-ligand})]^{+}$ precursors (M = Rh, Ir; cod = (*Z*,*Z*)-1,5-cyclooctadiene; and N-ligand is a podal bis(pyridyl)amine ligand: *N*,*N*-bis(2-pyridylmethyl)amine (dpa), *N*-(2-pyridylmethyl)-*N*-(6-methyl-2-pyridylmethyl)amine (pla), or *N*-benzyl-*N*,*N*-bis(6-methyl-2-pyridylmethyl)amine (Bn-dla). EPR spectroscopy, X-ray diffraction, and DFT calculations reveal that each of these $[M^{II}(cod)(N\text{-ligand})]^{2+}$ species adopts a square-pyramidal geometry with the two cod double bonds and the two pyridine fragments in the basal plane and the N_{amine} donor at the apical position. The unpaired electron of these species mainly resides at the metal center, but the apical N_{amine} donor also carries a considerable fraction of the total spin density (15–18%). Density functional calculations proved a valuable tool for the analysis and simulation of the experimental EPR spectra. Whereas the M^{II}(olefin) complexes are quite stable as solids, in solution they spontaneously transform into a 1:1 mixture of M^{III}(allyl) species and protonated M^{I}(olefin) complexes (in the forms $[M^{I}(olefin)(protonated\ N\text{-ligand})]^{2+}$ for M = Rh and $[M^{III}(H)(olefin)(N\text{-ligand})]^{2+}$ for M = Ir). Similar reactions were observed for the related propene complex $[M^{II}(propene)(Me_2tpa)]^{2+}$ (Me_2tpa = *N*,*N*,*N*-tris(6-methyl-2-pyridylmethyl)amine). The decomposition rate of the $[M^{II}(cod)(N\text{-ligand})]^{2+}$ species decreases with increasing N-ligand bulk in the following order: dpa > pla > Bn-dla. Decomposition of the most hindered $[M^{II}(cod)(Bn\text{-dla})]^{2+}$ complexes proceeds by a second-order process. The kinetic rate expression $v = k_{obs}[M^{II}]^2$ in acetone with $k_{obs} = k'[H^+][S]$, where [S] is the concentration of additional coordinating reagents (MeCN), is in agreement with ligand-assisted dissociation of one of the pyridine donors. Solvent coordination results in formation of more open, reactive species. Protonation of the noncoordinating pyridyl group increases the concentration of this species, and thus $[H^+]$ appears in the kinetic rate expression. The kinetic data are in agreement with bimolecular hydrogen-atom transfer from M^{II}(cod) to another M^{II} species ($\Delta H^{\ddagger} = 11.5 \pm 2\ \text{kcal mol}^{-1}$, $\Delta S^{\ddagger} = -27 \pm 10\ \text{cal K}^{-1}\text{mol}^{-1}$, and $\Delta G^{\ddagger}_{298\,K} = 19.5 \pm 5\ \text{kcal mol}^{-1}$).

Keywords: C−H activation · hydrogen transfer · iridium · N ligands · rhodium

Introduction

The organometallic chemistry of open-shell d^7 Rh^{II} and Ir^{II} complexes is quite fascinating and often leads to unexpected reaction pathways. With few exceptions, rhodium(II) complexes have been stabilized by preventing close contact of reagents or other rhodium(II) centers to the rhodium(II) center through coordinative saturation or application of ligands with sufficient steric bulk.[1] Less shielded rhodium(II) and iridium(II) species like $[M^{II}(por)]$ (M = Rh, Ir, por^{2-} = bulky *meso*-tetraarylporphyrinate) show remarkable reactivity towards a variety of otherwise rather inert substrates.[2] Activation under mild conditions of H_2, Si−H and Sn−H bonds, benzylic and allylic C−H bonds, and even methane have been reported. Apparently the $[M^{II}(por)]$ fragments

---

[a] D. G. H. Hetterscheid, M. Klop, Dr. R. J. N. A. M. Kicken,
J. M. M. Smits
Radboud University Nijmegen
Toernooiveld 1, 6525 ED Nijmegen (The Netherlands)

[b] Dr. E. J. Reijerse
Max-Planck-Institut für Bioanorganische Chemie
Stiftstrasse 34–36, 45470 Mülheim an der Ruhr (Germany)

[c] Dr. B. de Bruin
University of Amsterdam
van't Hoff Institute for Molecular Sciences (HIMS)
Department of Homogeneous and Supramolecular Catalysis
Nieuwe Achtergracht 166, 1018 WV Amsterdam (The Netherlands)
Fax: (+31) 20-525-6422
E-mail: BdeBruin@science.uva.nl

Supporting information for this article is available on the WWW under http://www.chemeurj.org/ or from the author.

behave as metalloradicals. This is clearly demonstrated by reactions with CO and ethene to give [M^{III}(por){μ_2-C(O)C(O)}M^{III}(por)], [M^{III}(por)(μ_2-CH_2CH_2)M^{III}(por)] and [(por)M^{III}(μ_2-$CH_2CH_2CH_2CH_2$)M^{III}(por)], and reactions with dihydrogen, toluene, and methane to give [M^{III}(por)(H)] and [M^{III}(por)(R)] (R = H, $CH_2C_6H_5$, CH_3). Formation of σ-allyl species [Rh^{III}($CH_2CR'{=}CR_2$)(por)] in 50% yield on reaction of porphyrinato complexes [Rh^{II}(por)] with olefins having allylic hydrogen atoms has also been reported.[3] In these reactions the fate of the remaining 50% of [Rh^{II}(por)] depends on the nature of the por^{2-} ligand: formation of alkyl species [Rh^{III}($CR_2CR_2CR_2H$)(por)] for less hindered porphyrins, and hydride species [Rh^{III}(H)(por)] for sterically more demanding porphyrins. Relevant to the work described in this paper, it has been suggested that these reactions may proceed via allylic C−H activation of M^{II}-(olefin) intermediates by M^{II} metalloradicals.[3c]

In the organometallic chemistry of second- and third-row transition metals, such hydrogen-atom abstractions are rare. Two-electron processes (e.g., oxidative addition, reductive elimination) dominate the chemistry of conventional P-ligand-supported rhodium(I) and rhodium(III) species.[4] Clearly, the reactivity of N-ligand-supported rhodium(II) and iridium(II) is very different, and this is the reason for our interest in the unusual behavior of M^{II}(olefin) radicals (M = Rh, Ir).

Recently we isolated Ir^{II}–ethene fragments supported by the N-ligands Me_ntpa ($n = 2, 3$).[4] In contrast to por^{2-} ligands, these amine-pyridine type N-ligands allow *cis* reactivity patterns. In addition, the much stronger binding of olefins to dicationic [M^{II}(N-ligand)]$^{2+}$ compared to neutral [M^{II}(por)] complexes allows more thorough investigation of the behavior of the olefin complexes. Coordination of a σ-donor ligand to 17-electron Ir^{II}(ethene) complexes leads to new species which are intermediate between a 19-VE iridium(II) metalloradical with a “slipped” ethene ligand and an 18-VE Ir^{III}–ethyl radical species.[5] This olefin “redox-non-innocent” behavior allows direct radical coupling between external $^3O_2$ and the olefinic substrate with subsequent formation of an aldehyde.[6] We have now further investigated the chemistry of nonporphyrinato N-ligand M^{II} olefin complexes. In this paper we report the synthesis and characterization of a series of [M^{II}(olefin)(N-ligand)]$^{2+}$ complexes containing olefins with allylic hydrogen atoms [M = Rh, Ir; olefin = propene, (*Z*,*Z*)-1,5-cyclooctadiene (cod)]. These species are not stable and decompose via allylic C−H activation of the olefin with formation of M^{III}(allyl) species.[7]

To the best of our knowledge, formation of M^{III}(allyl) species from M^{II}(cod) (M = Rh, Ir) has only been reported for [Rh^{II}(R_3-Cp)(cod)]$^+$ (R_3-Cp = tris-functionalized cyclopentadienyl ligand) generated in situ.[8] In this case, however, the mechanism was not thoroughly investigated, no spectroscopic evidence was presented for formation of a rhodium(II) intermediate, and no explanation was given for the mysterious loss of a hydrogen atom. Herein we present details of the C−H activation mechanism on the basis of kinetic studies following the decomposition of isolated M^{II}(cod) radicals.

Results and Discussion

Synthesis of the Rh^I and Ir^I cod complexes: We synthesized the cationic Rh^I and Ir^I cod complexes $\mathbf{1}^+$ and $\mathbf{2}^+$ by the routes shown in Scheme 1. Stirring *N*,*N*-bis(2-pyridylmethyl)amine (dpa) with [{M^I(μ-Cl)(cod)}$_2$] (M = Rh, Ir; cod = (*Z*,*Z*)-1,5-cyclooctadiene) in a molar ratio of 2:1 in methanol at room temperature (RT) results in formation of [**1**]Cl or [**2**]Cl. Addition of NH_4PF_6 to the solution of [**1**]Cl results in precipitation of [**1**]PF_6. To precipitate [**2**]PF_6, we used KPF_6 to prevent formation of iridium(III) hydrides.

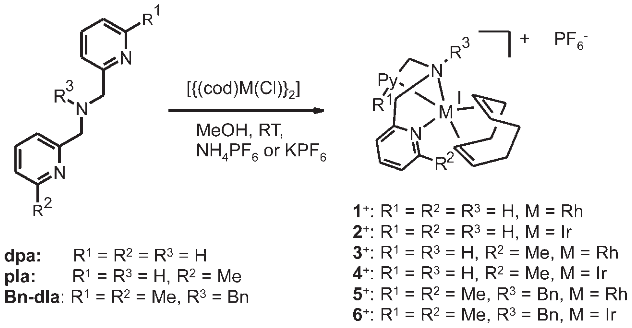

Scheme 1. Synthesis of M^I(cod) complexes $\mathbf{1}^+$–$\mathbf{6}^+$.

The analogous complexes $\mathbf{3}^+$–$\mathbf{6}^+$ were prepared in a similar manner starting from the ligands *N*-(2-pyridylmethyl)-*N*-(6-methyl-2-pyridylmethyl)amine (pla) and *N*-benzyl-*N*,*N*-bis(6-methyl-2-pyridylmethyl)amine (Bn-dla); see Scheme 1. Complexes $\mathbf{3}^+$ and $\mathbf{4}^+$ have methyl substituents at the Py-6 position which shield the metal from its environment. The steric shielding is most efficient in $\mathbf{5}^+$ and $\mathbf{6}^+$ containing two lutidyl donors. The amine nitrogen atom in $\mathbf{5}^+$ and $\mathbf{6}^+$ bears a benzyl substituent, which makes the amine a weaker donor. Complexes $\mathbf{1}^+$ and $\mathbf{5}^+$ were reported earlier, in a communication[7] and in a different context.[9]

X-ray structures of the M^I(cod) complexes: The X-ray structures of $\mathbf{1}^+$ and $\mathbf{5}^+$ have been reported previously.[7,9] Here we report the X-ray structures of $\mathbf{2}^+$, $\mathbf{3}^+$, $\mathbf{4}^+$, and $\mathbf{6}^+$. Selected bond lengths and angles are given in Tables 1 and 2.

Complexes [**5**]PF_6 and [**6**]PF_6 are isostructural, and for both $\mathbf{5}^+$ and $\mathbf{6}^+$ two independent, slightly different cations ($\mathbf{5_A}^+$ and $\mathbf{5_B}^+$, and $\mathbf{6_A}^+$ and $\mathbf{6_B}^+$, respectively) are found in the crystal lattice. For reasons of comparison we have included the distances and angles of the previously reported structure of [**5**]$^+$ in Tables 1 and 2.

The X-ray structures of cations $\mathbf{2}^+$ and $\mathbf{6}^+$ are shown in Figure 1. The structures of $\mathbf{3}^+$ and $\mathbf{4}^+$ are shown in Figures S1 and S2.

The coordination geometry of each of the complexes $\mathbf{2}^+$–$\mathbf{6}^+$ can be described as distorted trigonal-bipyramidal (tbpy). In this description, the N_{amine} donor (N3), one of the pyridine donors (N2), and a cod double bond (C5=C6) span the equatorial (trigonal) plane. The second pyridine donor

Table 1. Selected bond lengths [Å] and angles [°] of **2**$^+$, **3**$^+$, **4**$^+$, **5**$^+$, **5**$^{2+}$, and **6**$^+$.[a]

	[**2**]BPh_4	[**3**]BPh_4	[**4**]BPh_4	[**5A**]PF_6	[**5B**]PF_6	[**5**]$(PF_6)_2$	[**6A**]PF_6	[**6B**]PF_6
M−C1	2.134(9)	2.145(4)	2.131(9)	2.153(10)	2.161(10)	2.261(3)	2.146(7)	2.139(8)
M−C2	2.117(9)	2.163(3)	2.134(9)	2.183(10)	2.128(10)	2.242(3)	2.171(7)	2.134(8)
M−C5	2.068(7)	2.087(4)	2.099(9)	2.101(11)	2.104(11)	2.245(3)	2.093(8)	2.101(8)
M−C6	2.059(7)	2.084(5)	2.088(11)	2.096(10)	2.105(10)	2.222(3)	2.085(7)	2.103(7)
M−$X_{1,2}$	2.005	2.037	2.010	2.052	2.029	2.144	2.039	2.021
M−$X_{5,6}$	1.933	1.957	1.965	1.972	1.980	2.126	1.955	1.973
M−N1	2.092(6)	2.110(3)	2.099(7)	2.135(9)	2.138(8)	2.091(2)	2.135(6)	2.136(6)
M−N2	2.216(7)	2.222(4)	2.198(8)	2.282(8)	2.276(8)	2.102(2)	2.255(6)	2.247(6)
M−N3	2.232(6)	2.285(3)	2.255(8)	2.422(8)	2.408(7)	2.301(2)	2.368(5)	2.353(5)
C1−C2	1.410(17)	1.400(7)	1.423(14)	1.401(15)	1.385(16)	1.375(4)	1.412(11)	1.383(12)
C5−C6	1.445(13)	1.442(6)	1.446(13)	1.436(15)	1.427(15)	1.371(4)	1.475(11)	1.450(11)
N1-M-N2	83.5(2)	80.63(12)	80.3(3)	90.2(3)	87.3(3)	91.87(9)	90.4(2)	87.2(2)
N1-M-N3	78.2(2)	78.02(12)	77.5(3)	73.5(3)	73.5(3)	76.19(8)	74.5(2)	74.2(2)
N2-M-N3	74.6(2)	76.29(15)	76.5(3)	74.6(3)	75.2(3)	79.99(8)	75.9(2)	75.9(2)
N1-M-C1	156.9(3)	161.63(16)	160.3(3)	160.6(3)	160.0(4)	161.06(10)	161.8(3)	158.4(3)
N1-M-C2	164.4(4)	160.28(15)	160.7(3)	160.9(4)	161.7(4)	161.18(10)	159.0(3)	163.2(3)
N1-M-C5	95.8(3)	92.10(14)	93.0(3)	91.1(4)	92.4(4)	87.82(10)	90.5(3)	91.8(3)
N1-M-C6	90.2(3)	95.91(14)	96.4(3)	88.4(4)	88.0(4)	90.52(10)	87.1(3)	87.4(3)
N2-M-C1	113.5(3)	103.93(15)	105.8(3)	97.5(4)	100.2(4)	99.13(10)	98.2(3)	99.7(3)
N2-M-C2	84.6(4)	90.32(16)	91.3(3)	89.1(4)	92.2(4)	89.20(10)	88.9(3)	90.4(3)
N2-M-C5	159.1(3)	169.05(19)	167.8(4)	178.6(4)	178.7(4)	171.38(10)	178.1(3)	176.9(3)
N2-M-C6	119.7(3)	128.93(18)	127.7(4)	139.6(4)	139.1(4)	152.86(10)	137.0(3)	136.6(3)
N3-M-C1	90.9(3)	85.72(15)	85.7(3)	124.7(4)	125.3(4)	90.51(9)	125.5(3)	125.8(3)
N3-M-C2	108.2(3)	116.98(15)	117.7(3)	91.6(4)	92.1(4)	122.43(9)	92.0(3)	92.6(3)
N3-M-C5	123.6(3)	113.32(17)	114.4(4)	106.2(4)	105.9(4)	91.58(9)	106.0(3)	106.7(3)
N3-M-C6	164.1(3)	151.48(15)	152.6(4)	142.4(4)	141.0(3)	126.70(9)	143.1(3)	142.6(3)
C1-M-C2	38.7(5)	37.94(18)	39.0(4)	37.7(4)	37.7(4)	35.55(10)	38.2(3)	37.8(3)
C5-M-C6	41.0(4)	40.44(17)	40.4(4)	40.0(4)	39.6(4)	35.75(10)	41.4(3)	40.4(3)
C1-M-C5	97.4(4)	98.33(16)	97.6(4)	96.7(4)	96.8(4)	79.00(11)	97.3(3)	97.6(3)
C1-M-C6	81.4(4)	82.63(17)	81.3(4)	81.4(4)	80.5(4)	86.69(11)	81.4(3)	82.0(3)
C2-M-C5	78.8(3)	79.96(17)	78.4(4)	79.6(4)	80.2(4)	93.88(11)	79.2(3)	79.6(3)
C2-M-C6	89.2(4)	89.71(18)	88.2(4)	89.5(4)	88.7(4)	80.21(11)	89.7(3)	89.4(3)
N1-M-$X_{1,2}$	176.15	178.08	179.12	176.17	176.32	173.52	175.10	175.94
N2-M-$X_{1,2}$	99.34	97.45	98.99	93.46	95.93	94.38	93.74	95.35
N3-M-$X_{1,2}$	100.01	101.63	101.91	108.54	109.07	106.56	109.10	109.44
N1-M-$X_{5,6}$	93.22	94.26	94.97	89.76	90.24	80.12	88.68	89.59
N2-M-$X_{5,6}$	139.72	149.07	147.75	159.51	158.90	170.83	157.59	156.76
N3-M-$X_{5,6}$	144.05	132.79	133.95	124.77	123.96	109.08	125.13	125.19
$X_{1,2}$-M-$X_{5,6}$	86.26	87.36	85.91	86.41	86.12	84.44	86.50	86.81

[a] $X_{1,2}$ = centroid between C1 and C2; $X_{5,6}$ = centroid between C5 and C6.

(N1) and the other cod double bond (C1=C2) are coordinated axially (Figure 2).

The complexes cannot adopt ideal tbpy geometries due to the restricted bite angles of the N-CH_2-Py fragments. Thus, the most important deviations from ideal tbpy geometry are caused by the N2-M-N3 angles being too small for **2**$^+$–**6**$^+$. These fall in the range 74.6–80°, substantially smaller than 120° between the equatorial donors in ideal tbpy geometry. Consequently, the two remaining ligand–metal–ligand angles in the equatorial (trigonal) plane are substantially larger than 120° ($X_{5,6}$-M-N2 139.7–170.8, $X_{5,6}$-M-N3 124–144.1°, $X_{5,6}$ is the centroid of the C5=C6 double bond). The N1-M-$X_{1,2}$ angles defined by the axial donors N1 and the centroid of the C1=C2 double bond, which lie in the range 175.1–179.1°, are quite close to the ideal 180°.

As expected for d^8 metal centers in tbpy geometry,[10] the axial σ donors N1 (M−N1 2.092–2.138 Å) are more strongly bound than the equatorial σ donors. The equatorial M−N distances of the sp^2-hybridized Py donor N2 (M−N2 2.198–2.282 Å) are slightly shorter than those of the sp^3 N_{amine} donor N3 (M−N3 2.232–2.422 Å). As expected, for the pla complexes **3**$^+$ and **4**$^+$ the axial position is occupied by the strongest donor N_{Py}, and the weaker N_{PyMe} donor coordinates in the trigonal plane. For d^8 tbpy complexes, olefins tend to bind more strongly in the trigonal plane.[10] In good agreement, the M−C distances of the equatorial cod double bond (M−$X_{5,6}$ 1.933–1.980 Å) are shorter than those of the axial cod double bond (M−$X_{1,2}$ 2.005–2.052 Å). As a result of the stronger M–olefin interactions (stronger olefin→M σ bonding, stronger M→olefin π backbonding, and thus weakened C=C π bonding) in the equatorial (trigonal) plane, the C5−C6 distances (1.427–1.450 Å) are longer than the C1−C2 distances (1.383–1.423 Å). The C=C distance of the C5=C6 fragment is also long compared to those observed for other M^I(cod) fragments (M = Rh, Ir; only 66 structures in the Cambridge Structural Database have C=C distances longer than 1.438 Å, while more than 1350 structures have C=C distances shorter than 1.437 Å). The M−C5=C6 fragment thus seems to have a significant metalla(III)cyclopropane character. As such, one could perhaps describe the species

Table 2. Crystallographic data for [**1H**]$(PF_6)_2$, [**2**]BPh_4, [**3**]BPh_4, [**4**]BPh_4, [**5**]$(PF_6)_2$, [**6**]PF_6, [**10**]$(PF_6)_2$, and [**11**]$(PF_6)_2$.

	[**1H**]$(PF_6)_2$-$\cdot$0.5 CH_2Cl_2	[**2**]BPh_4	[**3**]BPh_4	[**4**]BPh_4	[**5**]$(PF_6)_2$	[**6**]PF_6	[**10**]$(PF_6)_2$-$\cdot$dioxane	[**11**]$(PF_6)_2$-$\cdot$dioxane
crystal color	transparent light brown	translucent bright yellow	translucent yellow-brown	translucent yellow	translucent green	translucent yellow-light brown	transparent light yellow	translucent colorless
crystal shape	rather regular fragment	regular fragment	irregular lump	irregular lump	rough lump	irregular lump	regular fragment	regular fragment
crystal size [mm]	0.42×0.21 ×0.18	0.42×0.28 ×0.14	0.24×0.22 ×0.16	0.52×0.44 ×0.22	0.24×0.21 ×0.21	0.50×0.27 ×0.23	0.42×0.21 ×0.18	0.30×0.28 ×0.13
formula	$C_{20.5}H_{27}ClF_{12}$-N_3P_2Rh	$C_{44}H_{45}BIrN_3$	$C_{45}H_{47}BN_3Rh$	$C_{45}H_{47}BIrN_3$	$C_{33}H_{45}F_{12}N_3OP_2Rh$	$C_{32}H_{41}F_6IrN_3OP$	$C_{24}H_{32}F_{12}N_3O_2P_2Rh$	$C_{24}H_{34}F_{12}IrN_3O_2P_2$
M_r	743.75	818.84	743.58	832.87	892.57	820.85	787.38	878.68
T [K]	293.(2)	293(2)	293(2)	208(2)	293(2)	173(2)	293(2)	150(2)
radiation	Cu_K	Cu_K	Cu_K	Cu_K	Mo_K	Cu_K	Mo_K	Mo_K
λ [Å]	1.54184	1.54184	1.54184	1.54184	0.71073	1.54184	0.71073	0.71073
crystal system	monoclinic	orthorhombic	monoclinic	monoclinic	monoclinic	monoclinic	monoclinic	triclinic
space group	$C2/c$	$P2_12_12_1$	$P2_1$	$P2_1$	$P2_1/n$	$P21$	$P2_1/c$	$P\bar{1}$
unit cell dimensions[a]								
a [Å]	32.085(9)	4.103(3)	11.2125(5)	11.1920(7)	10.9046(2)	10.4174	10.9720(12)	9.8945(4)
b [Å]	10.0677(11)	17.0055(3)	10.0170(6)	9.9916(13)	17.1600(13)	25.1229(9)	15.514(3)	10.7143(11)
c [Å]	18.052(4)	22.1838(6)	16.6033(10)	16.6579(12)	19.8594(10)	12.1147(4)	18.2190(18)	14.3611(15)
α [°]	90	90	90	90	90	90	90	91.180(10)
β [°]	108.30(2)	90	103.049	103.230	105.346(3)	101.013	100.562(10)	102.973(6)
γ [°]	90	90	90	90	90	90	90	97.691(7)
V [Å^3]	5537(2)	3550.01(16)	1816.64(18)	1813.3(3)	3583.7(3)	3112.22(19)	3048.7(7)	1668.2(2)
Z	8	4	2	2	4	4	4	2
ρ_{calcd} [$Mg\,m^{-3}$]	1.785	1.532	1359	1.525	1654	1.752	1.715	1.988
μ [mm^{-1}]	7.897	7.543	4.066	7.394	0.662	9.382	0.767	4.762
diffractometer	Enraf-Nonius CAD4	Enraf-Nonius CAD4	Enraf-Nonius CAD4	Enraf-Nonius CAD4	Nonias KappaCCD[b]	Enraf-Nonius CAD4	Enraf-Nonius CAD4	Nonias KappaCCD[b]
scan	$\omega-2\theta$	$\omega-2\theta$	$\omega-2\theta$	$\omega-2\theta$	ϕ and ω	$\omega-2\theta$	$\omega-2\theta$	ϕ and ω
F(000)	2968	1648	776	840	1820	1632	1584	860
θ range [°]	2.90–69.94	3.27–69.96	2.73–69.91	2.72–69.84	2.27–27.50	3.52–69.91	2.71–27.51	5.08–27.50
index ranges	$-38 \leq h \leq 14$ $-12 \leq k \leq 3$ $-20 \leq l \leq 21$	$0 \leq h \leq 11$ $0 \leq k \leq 20$ $0 \leq l \leq 27$	$13 \leq h \leq 13$ $-12 \leq k \leq 12$ $-20 \leq l \leq 20$	$-13 \leq h \leq 13$ $-12 \leq k \leq 0$ $0 \leq l \leq 20$	$-14 \leq h \leq 14$ $-22 \leq k \leq 22$ $-25 \leq l \leq 25$	$-12 \leq h \leq 12$ $-30 \leq k \leq 0$ $-14 \leq l \leq 0$	$-14 \leq h \leq 0$ $-20 \leq k \leq 0$ $-23 \leq l \leq 23$	$-12 \leq h \leq 12$ $-13 \leq k \leq 13$ $-18 \leq l \leq 18$
reflns collected/unique	5358/5248	3786/3786	7325/6647	3775/3648	62 040/8197	6331/6039	7347/6992	46 846/6685
R(int)	0.1008	0.0000	0.0481	0.0561	0.0374	0.0210	0.0255	0.0348
reflns obsd [$I_o > 2\sigma(I_o)$]	3457	3744	6552	3646	6745	6019	3739	6203
data/restraints/parameters	5248/0/369	3786/0/443	6647/1/452	3648/781/453	8197/0/426	6039/1/801	6992/0/412	6685/0/400
GOF on F^2	1.030	1.081	1.066	1.176	1.062	1.070	1.040	1.083
SHELXL-97 weight parameters	0.0821, 29.0865	0.0591, 5.1565	0.0800, 1.3351	0.0840, 5.9058	0.0294, 5.7470	0.0544, 8.1951	0.1166, 3.691	0.0155, 1.6716
final R indices [$I > 2\sigma(I)$]								
$R1$	0.0617	0.0331	0.0371	0.0430	0.0411	0.0281	0.0791	0.0180
$wR2$	0.1578	0.0890	0.1063	0.1205	0.0812	0.0760	0.1951	0.0412
R indices (all data)								
$R1$	0.0946	0.0334	0.0375	0.0430	0.0572	0.0282	0.1564	0.0215
$wR2$	0.1792	0.0892	0.1068	0.1205	0.0866	0.0761	0.2381	0.0422
largest diff. peak/hole [$e\,Å^{-3}$]	0.685/−0.587	1.893/−2.176	0.787/−1.172	2.422/−2.917	0.966/−0.372	1.798/−2.304	1.508/−0.592	0.985/−0.615

[a] Based on 25 reflections ($40.020 < \theta < 46.446$). [b] With area detector.

as metal(III) complexes in which the C5=C6 fragment is reduced by two electrons. In this description, the geometry is better described as distorted octahedral, with C5 and C6 of the metalla(III)cyclopropane moiety coordinated approximately *trans* to N2 and N3, respectively (N2-M-C5 159.1–178.6, N3-M-C6 141.0–164.1°). This is depicted as one of the limiting resonance structures in Figure 2.

Table 1 reveals that the M−N and M−C distances at comparable axial, basal, and equatorial positions are consistently shorter for the iridium complexes compared to their rhodi-

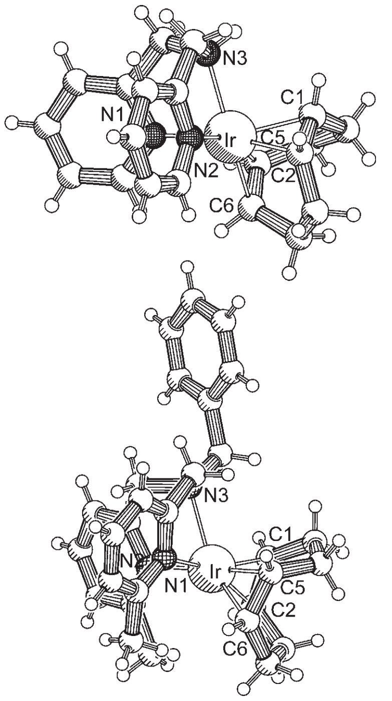

Figure 1. X-ray structures of 2^+ (top) and $6_A{}^+$ (bottom). Rh^I(cod) complex $5_A{}^+$ is isostructural to Ir^I(cod) complex $6_A{}^+$.

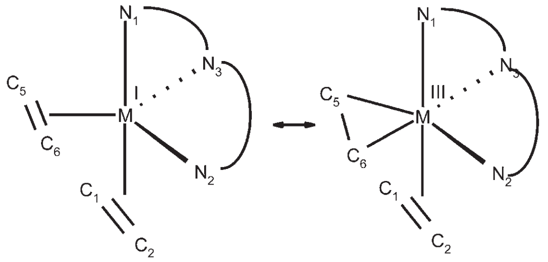

Figure 2. Limiting resonance structures describing the M(cod) species as distorted tbpy M^I(cod) and distorted octahedral metalla(III)cyclopropane olefin complexes.

um analogues. This could be meaningful, despite the fact that the observed differences are not significant and fall within the experimental errors (3σ criterion).

Cyclic voltammetry: Electrochemical oxidation of 1^+–6^+ was investigated by cyclic voltammetry in dichloromethane and acetone. All complexes, except for 2^+ and 6^+, exhibit electrochemically reversible M^I/M^{II} redox couples in acetone and dichloromethane. Complex 6^+ only reveals a reversible 1+/2+ couple in acetone. In dichloromethane, oxidation to 6^{2+} seems to be followed by a rapid reaction with the solvent. Oxidation of 2^+ to 2^{2+} proved irreversible in both acetone and dichloromethane.

The anodic peak potentials (E_a), half-wave potentials ($E_{1/2}$), and peak separation (ΔE) of the observed redox couples are summarized in Table 3. The redox potential (comparing $E_{1/2}$ values) at which one-electron oxidation of M^I to M^{II} occurs lies about 70–100 mV lower for M = Ir than for M = Rh. Apparently, the $[Ir^I(cod)(N\text{-ligand})]^+$ complexes are more prone to oxidation than their rhodium analogues.

Table 3. Electrochemical data for complexes **1**–**6**.[a]

Complex	Solvent	E_a [mV]	ΔE [mV]	$E_{1/2}$ [mV]	I_f/I_b	ΔG^0_{disp} [kcal mol^{-1}]
[**1**]PF_6	CH_2Cl_2	119	66	86	0.9	>29
[**1**]PF_6	acetone	93	123	31	0.9	>22
[**2**]PF_6	CH_2Cl_2	50	68	16	0.6	>31
[**2**]PF_6	acetone	89	–	–	0	–
[**3**]PF_6	CH_2Cl_2	140	65	108	1.0	>29
[**3**]PF_6	acetone	70	78	31	1.0	>22
[**4**]PF_6	CH_2Cl_2	56	60	26	1.0	>31
[**4**]PF_6	acetone	5	70	–30	1.0	>24
[**5**]PF_6	CH_2Cl_2	341	68	307	1.0	>24
[**5**]PF_6	acetone	247	88	203	1.0	>18
[**6**]PF_6	CH_2Cl_2	251	–	–	0	–
[**6**]PF_6	acetone	155	94	108	1.0	>21

[a] E_p = anodic peak potential, $E_{1/2}$ = half-wave potential, ΔE: peak separation, I_b/I_f = cathodic peak current/anodic peak current. Scan rate 100 mV s^{-1}.

The redox potentials of the M^{II}/M^{III} couples could not be observed. The solvent (acetone: above 1000 mV versus Fc/Fc$^+$; dichloromethane: above 1350 mV versus Fc/Fc$^+$) is oxidized at lower potentials than the M^{II} species. These data allow us to conclude that the $[M^{II}(cod)(N\text{-ligand})]^{2+}$ species are stable towards electron-transfer disproportionation at room temperature. The ΔG^0_{disp} values in Table 3 represent a lower-limit approximation of the thermodynamic energies associated with disproportionation of the M^{II} species to M^I and M^{III}, which is determined for each complex via $\Delta G^0_{disp} = -F(E^{1+/2+}_{1/2} - E^{2+/3+}_{1/2})$ by using the measured $E^{1+/2+}_{1/2}$ value of the 1+/2+ couple and the upper boundary of the solvent potential window (1350 mV for CH_2Cl_2, 1000 mV for acetone) as a lower limit for $E^{2+/3+}_{1/2}$. Disproportionation of the M^{II} species is strongly endergonic. The large ΔG^0_{disp} values suggest that direct electron-transfer disproportionation might not occur at measurable rates at room temperature or below. The unfavorable formation of 3+ charged species for these relatively small species could be a contributing factor to the unusual stability of the M^{II} species with respect to electron-transfer disproportionation.

It further follows from Table 3, as a global trend, that the ease of oxidation of the complexes decreases in the order dpa ~ pla > Bn-dla. This order correlates with the fact that (for steric reasons) these ligands become weaker donors when they are functionalized at the amine or the pyridine 6-positions.[11]

Synthesis of M^{II}(cod) metalloradicals: The electrochemical data reveal that $[M^{II}(cod)(N\text{-ligand})]^{2+}$ species have a measurable lifetime. To study their behavior, we synthesized these species on a preparative scale.

Complexes 1^{2+} and 4^{2+} were obtained by oxidation of 1^+ and 4^+ with [Fc]PF_6 in dichloromethane, which resulted in precipitation of [**1**]$(PF_6)_2$ and [**4**]$(PF_6)_2$. Oxidation of 2^+ to

$\mathbf{2}^{2+}$ is electrochemically irreversible, but complex $\mathbf{2}^{2+}$ could nevertheless be obtained by oxidation of $\mathbf{2}^{+}$ with [Fc]PF_6 in dichloromethane because the product [**2**]$(PF_6)_2$ rapidly precipitates from the solution. Complexes $\mathbf{3}^{2+}$, $\mathbf{5}^{2+}$, and $\mathbf{6}^{2+}$ were obtained by oxidation of $\mathbf{3}^{+}$, $\mathbf{5}^{+}$, and $\mathbf{6}^{+}$ with $AgPF_6$ in acetone (Scheme 2), followed by addition of diethyl ether to precipitate [**3**]$(PF_6)_2$, [**5**]$(PF_6)_2$, and [**6**]$(PF_6)_2$, respectively. We reported a similar procedure for the preparation of [Rh^{II}(norbornadiene)(pla)]$(PF_6)_2$.[11]

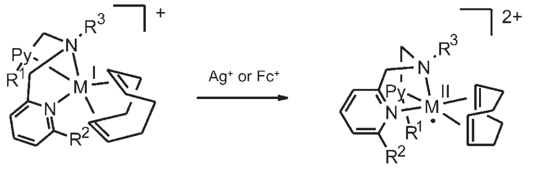

$\mathbf{1}^{+}$: $R^1 = R^2 = R^3 = H$, M = Rh
$\mathbf{2}^{+}$: $R^1 = R^2 = R^3 = H$, M = Ir
$\mathbf{3}^{+}$: $R^1 = R^3 = H$, $R^2 = Me$, M = Rh
$\mathbf{4}^{+}$: $R^1 = R^3 = H$, $R^2 = Me$, M = Ir
$\mathbf{5}^{+}$: $R^1 = R^2 = Me$, $R^3 = Bn$, M = Rh
$\mathbf{6}^{+}$: $R^1 = R^2 = Me$, $R^3 = Bn$, M = Ir

$\mathbf{1}^{2+}$: $R^1 = R^2 = R^3 = H$, M = Rh
$\mathbf{2}^{2+}$: $R^1 = R^2 = R^3 = H$, M = Ir
$\mathbf{3}^{2+}$: $R^1 = R^3 = H$, $R^2 = Me$, M = Rh
$\mathbf{4}^{2+}$: $R^1 = R^3 = H$, $R^2 = Me$, M = Ir
$\mathbf{5}^{2+}$: $R^1 = R^2 = Me$, $R^3 = Bn$, M = Rh
$\mathbf{6}^{2+}$: $R^1 = R^2 = Me$, $R^3 = Bn$, M = Ir

Scheme 2. Synthesis of M^{II}(cod) complexes $\mathbf{1}^{2+}$–$\mathbf{6}^{2+}$.

X-ray structure of Rh^{II}(cod) complex $\mathbf{5}^{2+}$: Complex $\mathbf{5}^{2+}$ proved to be sufficiently stable to grow crystals suitable for X-ray diffraction. These were obtained from a solution of [**5**]$(PF_6)_2$ in acetone at −20°C overlayered with diethyl ether. The X-ray structure of the dicationic Rh^{II} species $\mathbf{5}^{2+}$ is shown in Figure 3.

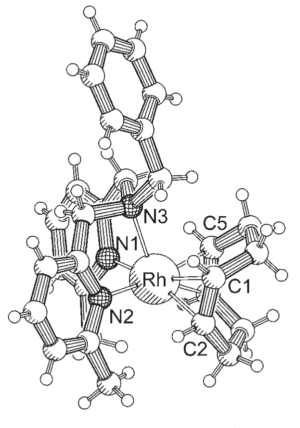

Figure 3. X-ray structure of Ir^{II}(cod) complex $\mathbf{5}^{2+}$.

Whereas $\mathbf{5}^{+}$ is best described as a trigonal bipyramid (vide supra), the coordination geometry of $\mathbf{5}^{2+}$ is best described as distorted square-pyramidal (sqpy). The amine occupies the apical position and the pyridine and olefin moieties are coordinated in the basal plane, with the N1 and N2 pyridine donors coordinated approximately *trans* to the C1=C2 (with centroid $X_{1,2}$) and C5=C6 (with centroid $X_{5,6}$) bonds (N1-M-$X_{1,2}$ = 173.5°, N2-M-$X_{5,6}$ = 170.8°). The most important deviations from the ideal sqpy geometry are caused by the restricted N-CH_2-Py bite angles, which cause the N3-M-N1 (76.2°) and N3-M-N2 (80.0°) angles to be somewhat too small and thus result in somewhat too large N3-M-$X_{1,2}$ (106.6°) and N3-M-$X_{5,6}$ (109.1°) angles. Twisting of the methylene bridges results in a slightly asymmetric complex.

Oxidation of $\mathbf{5}^{+}$ to $\mathbf{5}^{2+}$ results in stronger binding of the Bn-dla ligand to Rh; the Rh−N3 (N_{amine}) and the Rh−N2 (N_{PyMe}) distances shorten by about 0.11 Å and 0.18 Å respectively, whereas the N1−Rh (N_{PyMe}) distance does not change significantly (See Table 1). The slight shortening of the C1−C2 and C5−C6 distances (by ca. 0.04 Å) and the significant elongation of the Rh−C bonds (ca. 0.12 longer M−$X_{1,2}$ and M−$X_{5,6}$ distances) on going from $\mathbf{5}^{+}$ to $\mathbf{5}^{2+}$ indicates weakening of the Rh–olefin interactions on oxidation of Rh^{I} to Rh^{II}. This must be caused by decreased Rh→olefin π backbonding in $[\mathbf{5}]^{2+}$ compared to $[\mathbf{5}]^{+}$.[11]

DFT geometry optimizations of the M^{II}(cod) complexes: The sterically less hindered M^{II}(cod) complexes $\mathbf{1}^{2+}$–$\mathbf{4}^{2+}$ proved to be too unstable to grow X-ray-quality crystals. Therefore, we used DFT methods to obtain geometrical information on these complexes.

Due to the Jahn–Teller effect, trigonal-bipyramidal start geometries of complexes $\mathbf{1}^{2+}$-$\mathbf{6}^{2+}$ are not stable and converge to (distorted) square-pyramidal geometries, invariably with the two double bonds of cod in the basal plane. We optimized the geometry of the conformational local minima shown in Figure 4, each of which has a different N donor of the dpa, pla, or Bn-dla ligand occupying the apical position. For all complexes, the most stable geometries are found to be the square pyramids A and A^T with N_{amine} (N3) at the apical position. In square pyramids A, the N-CH_2-Py methylene fragments adopt a symmetrical arrangement. In square pyramids A^T the N-CH_2-Py methylene fragments have a twisted arrangement in which bending of one of the methylene fragments towards the other leads to a structure similar to the X-ray structure of $\mathbf{5}^{2+}$ (see Figure 3). The energies of geometries A and A^T do not differ much. For complexes $\mathbf{1}^{2+}$–$\mathbf{4}^{2+}$ with dpa and pla ligands, the twisted conformations A^T are not local minima and converge to the symmetrical A geometries. For the Bn-dla complexes $\mathbf{5}^{2+}$ and $\mathbf{6}^{2+}$ the twisted A^T geometries are about 0.7 $kcal\,mol^{-1}$ more stable than the A geometries (in good agreement with the X-ray structure of $\mathbf{5}^{2+}$).

Geometries B and C with N_{Py} or N_{PyMe} donors (N1 and N2) at the apical positions are 4–12 $kcal\,mol^{-1}$ higher in energy (Figure 4) than the corresponding A or A^T geometries. They also have longer average M−N distances (Table 4). Geometries B and C are clearly accessible at room temperature, but geometries A and A^T should be most relevant to the experimental EPR measurements in frozen solutions. Therefore, we used only the A and A^T geometries as input to calculate the EPR parameters of $\mathbf{1}^{2+}$–$\mathbf{6}^{2+}$ (see below).

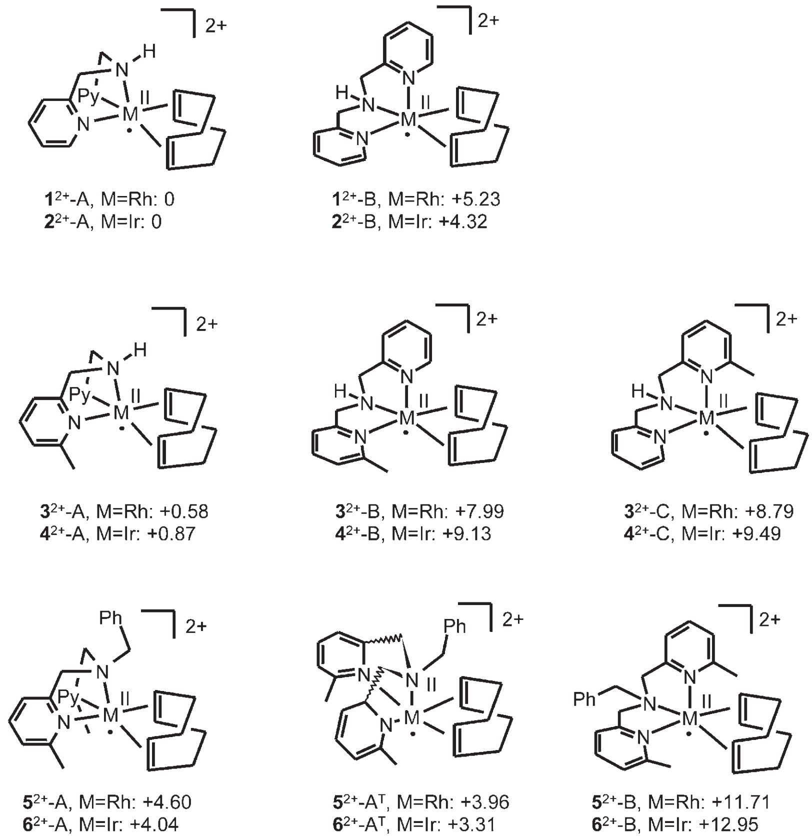

1^{2+}-A, M=Rh: 0
2^{2+}-A, M=Ir: 0

1^{2+}-B, M=Rh: +5.23
2^{2+}-B, M=Ir: +4.32

3^{2+}-A, M=Rh: +0.58
4^{2+}-A, M=Ir: +0.87

3^{2+}-B, M=Rh: +7.99
4^{2+}-B, M=Ir: +9.13

3^{2+}-C, M=Rh: +8.79
4^{2+}-C, M=Ir: +9.49

5^{2+}-A, M=Rh: +4.60
6^{2+}-A, M=Ir: +4.04

5^{2+}-A^{T}, M=Rh: +3.96
6^{2+}-A^{T}, M=Ir: +3.31

5^{2+}-B, M=Rh: +11.71
6^{2+}-B, M=Ir: +12.95

Figure 4. Relative energies (kcal mol^{-1}, b3-lyp) of the square-pyramidal conformations of complexes $\mathbf{1}^{2+}$–$\mathbf{6}^{2+}$ as obtained by DFT calculations. For easy comparison, the energy of the free N-ligand has been subtracted from the energy of the complex.

Table 4. Calculated (DFT) metal–nitrogen bond lengths [Å] for the complexes $\mathbf{1}^{2+}$–$\mathbf{6}^{2+}$ in the different conformations A, A^{T}, B, and C (see Figure 4).

	M	M–N3 (N_{amine})	M–N2 (N_{Py}/N_{PyMe})	M–N1 (N_{Py}/N_{PyMe})	M–N_{av}
$\mathbf{1}^{2+}$-A	Rh	2.291[a]	2.117	2.112	2.174
$\mathbf{1}^{2+}$-B	Rh	2.159	2.236[a]	2.132	2.176
$\mathbf{2}^{2+}$-A	Ir	2.317[a]	2.137	2.131	2.195
$\mathbf{2}^{2+}$-B	Ir	2.194	2.258[a]	2.144	2.199
$\mathbf{3}^{2+}$-A	Rh	2.278[a]	2.111	2.147 (N_{PyMe})	2.179
$\mathbf{3}^{2+}$-B	Rh	2.136	2.231[a]	2.191 (N_{PyMe})	2.186
$\mathbf{3}^{2+}$-C	Rh	2.160	2.114	2.356[a] (N_{PyMe})	2.210
$\mathbf{4}^{2+}$-A	Ir	2.305[a]	2.130	2.165 (N_{PyMe})	2.200
$\mathbf{4}^{2+}$-B	Ir	2.166	2.243[a]	2.207 (N_{PyMe})	2.205
$\mathbf{4}^{2+}$-C	Ir	2.184	2.132	2.376[a] (N_{PyMe})	2.231
$\mathbf{5}^{2+}$-A	Rh	2.400[a]	2.155 (N_{PyMe})	2.165 (N_{PyMe})	2.240
$\mathbf{5}^{2+}$-A^{T}	Rh	2.393[a]	2.171 (N_{PyMe})	2.164 (N_{PyMe})	2.243
$\mathbf{5}^{2+}$-B	Rh	2.203	2.184 (N_{PyMe})	2.406[a] (N_{PyMe})	2.264
$\mathbf{6}^{2+}$-A	Ir	2.404[a]	2.183 (N_{PyMe})	2.172 (N_{PyMe})	2.253
$\mathbf{6}^{2+}$-A^{T}	Ir	2.404[a]	2.181 (N_{PyMe})	2.177 (N_{PyMe})	2.254
$\mathbf{6}^{2+}$-B	Ir	2.228	2.203 (N_{PyMe})	2.413[a] (N_{PyMe})	2.281

[a] Apical position.

According to Rossi and Hoffmann, d^7 metals in a square-pyramidal geometry have a tendency to form stronger basal σ bonds than apical σ bonds, although this tendency should be reduced compared to their d^8 analogues.[10] Indeed, as shown in Table 4, the calculated M–N_{basal} bond lengths of complexes $\mathbf{1}^{2+}$–$\mathbf{6}^{2+}$ are consistently shorter than the M–N_{apical} bond lengths in each of the conformations A, A^{T}, B, and C.

The decreasing donor capacity of the ligands in the order dpa > pla > Bn-dla is clearly illustrated by longer corresponding average M–N distances, both for the Rh^{II}(cod) and the Ir^{II}(cod) complexes. The relative energy of the complexes increases accordingly (see Figure 4). This must be for steric reasons.[11]

EPR spectroscopy and electronic structure: We measured the X-band EPR spectra of isolated complexes $\mathbf{1}^{2+}$–$\mathbf{6}^{2+}$ in frozen acetone solution at temperatures between 20 and 40 K. Tetra-*n*-butylammonium hexafluorophosphate was added to improve the quality of the spectra. Two representative spectra, those of iridium complex $\mathbf{4}^{2+}$ and rhodium complex $\mathbf{5}^{2+}$, are shown in Figure 5. Complex $\mathbf{2}^{2+}$ is so reactive that we were unable to obtain an EPR spectrum of this species in frozen solution. However, we obtained spectra of reasonable quality directly from the solid material at 20 K.

All spectra could be satisfactorily simulated as rhombic spectra, with well-resolved (super)hyperfine interactions (HFI) with the metal center and a single nitrogen atom along the $g_3(z)$ axis. The $g_1(x)$ and $g_2(y)$ signals of rhodium(II) complexes $\mathbf{1}^{2+}$ and $\mathbf{3}^{2+}$ are not well separated, and these spectra could in principle also be simulated by assuming axial spectra. However, simulations with a rhombic g tensor with somewhat smaller line widths resulted in a slightly better fit. For all other complexes the rhombicity is unambiguous, with well-separated $g_1(x)$ and $g_2(y)$ signals. The EPR parameters obtained from spectral simulation are listed in Table 5.

As expected for heavier transition metals with larger spin–orbit couplings, the g anisotropy (rhombicity) of the iridium complexes is larger than that of the rhodium complexes. The iridium HFIs are also larger than the rhodium HFIs. The $A_1^{N}(x)$ and $A_2^{N}(y)$ values are not significant, since no resolved nitrogen HFIs were observed along the $g_1(x)$ and $g_2(y)$ axes in the experimental spectra. Likewise $A_1^{Rh}(x)$, $A_2^{Rh}(y)$ and $A_1^{Ir}(x)$, $A_2^{Ir}(y)$ are only upper limits, since no resolved metal HFIs were observed along the $g_1(x)$ and $g_2(y)$ axes.

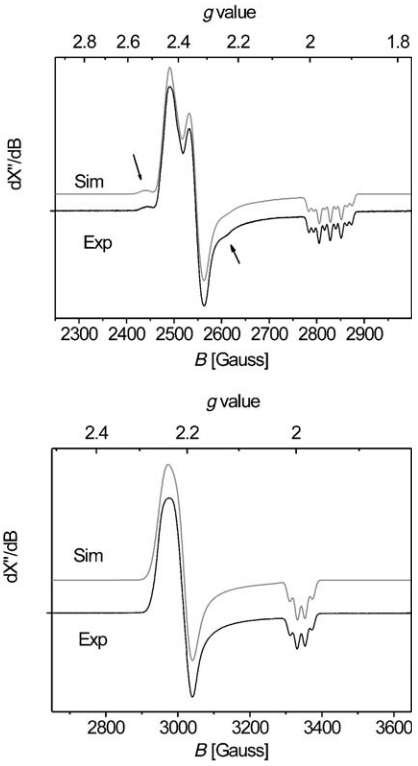

Figure 5. Experimental and simulated EPR spectra of Ir^{II} complex $\mathbf{4}^{2+}$ (top) and Rh^{II} complex $\mathbf{5}^{2+}$ (bottom) in frozen acetone/TBAH at 20 K. Modulation amplitude = 4 G, attenuation = 30 dB. The simulations were obtained with the parameters listed in Table 5. The arrows in the top spectrum indicate the "forbidden" $\Delta M_I = 2$ transitions, weakly allowed by strong mixing of the Ir NQI.

The EPR spectra of the M^{II} complexes with g_x, $g_y > 2$, $g_z \approx 2$, and g_z exhibiting strong (super)hyperfine coupling with both the metal and the apical N_{amine} donor (Table 5) are indicative for a mainly d_{z^2}-based SOMO,[12] in good agreement with the DFT calculations (vide infra). For all Ir^{II} compounds (Table 5) the g_z value is notably smaller than g_e, and this points to some small mixing of the d_{z^2} orbital with (an)other d orbital(s) in the SOMO.

In simulations of EPR powder spectra of quadrupolar first- and second-row transition metals, the quadrupole interaction (NQI) term $I{\cdot}Q{\cdot}I$ is usually neglected in the spin Hamiltonian, because it contributes only marginally to the spectral fine structure. However, in our case the NQI is comparable to the iridium HFI and therefore this approximation is no longer valid. The NQI causes the appearance of two weak "forbidden" ($\Delta m_I = 2$) transitions along the $g_1(x)$ axis in the EPR spectra of $\mathbf{4}^{2+}$ and $\mathbf{6}^{2+}$. For complex $\mathbf{4}^{2+}$ these are indicated by arrows in Figure 5. We have previously observed a similar effect in the EPR spectrum of $[Ir^{II}(ethene)(Me_3tpa)]^{2+}$.[5] Recently, Rieger et al.,[13] who studied $[Ir^{II}(Tp')(CO)(PPh_3)]^+$ (Tp' = hydrotris(3,5-dimethylpyrazolyl)borate) and other related paramagnetic iridium compounds, also required inclusion of the quadrupole term to simulate the EPR spectra of these compounds. In their case the "quadrupole effect" did not lead to the observation of "forbidden" transitions, but merely to shifts and intensity redistributions within the HFI multiplet.

The simulated spectrum in Figure 5 was generated by using the best-fit spectral parameters listed in Table 5. All interaction tensors are assumed to coincide (same principle axes). The simulation shows the additional "forbidden" satellites at the $g_1(x)$ position, which allows an accurate determination of the iridium NQI along the $g_3(z)$ axis. The NQI rhombicity parameter η was set to zero, but variation up to $\eta = 0.2$ has little influence on the simulation.

To obtain more information about the experimental spectra, we also calculated the EPR parameters of the optimized lowest energy A and A^T conformations of complexes $\mathbf{1}^{2+}$–$\mathbf{6}^{2+}$ using DFT methods. The results are listed in Table 5. For all complexes, the A and A^T conformations give rise to rhombic spectra according to the DFT calculations. The difference between $g_1(x)$ and $g_2(y)$ is expected to be bigger for the A^T geometries. This is predicted by DFT, but the calculated rhombicity of the A^T geometries is not much larger than the rhombicity of the A geometries. Although the cod fragments are bound in a slightly twisted way and the two $M{-}N_{Py}$ distances are not equal, this is not the main reason for observing rhombic g values. The rhombicity in the DFT calculations is mainly caused by the fact that the g-tensor axes do not coincide with the molecular bond axes of the square pyramid. In fact, for all these $[M^{II}(cod)(N\text{-}ligand)]^{2+}$ complexes, the principle axes of the g tensor lie as depicted in Figure 6. The $g_1(x)$ axis follows the pseudo mirror plane of the complex, in between the two N_{Py} donors and the two cod double bonds. The $g_2(y)$ axis also lies in the square plane defined by the two N_{Py} and the two cod donors at about 45° with respect to the $M{-}N_{Py}$ and the metal–olefin bond axes. The $g_3(z)$ axis points towards the axial position of the square pyramid, and slightly deviates from the direction of the $M{-}N_{amine}$ bond. The experimental directions of the principle axes of the g tensor should match those of the DFT calculations, and this gives a good explanation for the fact that changing the symmetrical dpa ligand in $\mathbf{1}^{2+}$ to the nonsymmetrical pla ligand in $\mathbf{3}^{2+}$ has virtually no effect on the g anisotropy.

The agreement between the experimental and calculated g values is remarkable, considering the presence of the heavy rhodium and iridium centers, which usually degrade the accuracy of DFT property calculations. The $g_3(z)$ components of the metal–electron HFI is slightly overestimated, but apart from that, the calculated rhodium, iridium, and N_{amine} HFIs represent the experimental data quite well. The large NQI interactions observed for the iridium compounds are also well predicted by the calculations.

For each of the complexes $\mathbf{1}^{2+}$–$\mathbf{6}^{2+}$, DFT spin density plots reveal that the spin density is substantially delocalized over the N_{amine} donor and the metal atom, with the main part residing at the metal (Figure 7). Mulliken spin density populations from the DFT calculations at these nuclei are included in Table 5. For the N_{amine} donors, these populations range from 15 to 18 %, and these donors are responsible for the observed large nitrogen HFIs of about 60 MHz along

Table 5. Simulation (Exptl) and DFT calculated EPR parameters (MHz) of $[M^{II}(cod)(N\text{-ligand})]^{2+}$ compounds $\mathbf{1}^{2+}$–$\mathbf{6}^{2+}$ (Scheme 1).[a]

Compound		$g_1(x)$		$g_2(y)$		$g_3(z)$	
		Exptl	DFT	Exptl	DFT	Exptl	DFT
$\mathbf{1}^{2+}$	g value	2.227	2.204	2.203	2.188	2.011	1.985
M=Rh	HFI_{Rh} (sd)	<60	18	<60	22	61	87 (76 %)
N-ligand=dpa	$HFI_{N\text{-amine}}$ (sd)	<60	35	<60	35	61	58 (15 %)
$\mathbf{2}^{2+}$	g value	2.450	2.478	2.360	2.397	1.950	1.888
M=Ir	HFI_{Ir} (sd)	<130	114	<130	121	130	185 (78 %)
N-ligand=dpa	$HFI_{N\text{-amine}}$ (sd)	<130	35	<130	35	60	58 (15 %)
	NQI (η)	nr	−76	nr	−51	nr	127 (0.20)
$\mathbf{3}^{2+}$	g value	2.221	2.200	2.195	2.178	2.010	1.986
M=Rh	HFI_{Rh} (sd)	<60	17	<60	11	61	81 (77 %)
N-ligand=pla	$HFI_{N\text{-amine}}$ (sd)	<60	35	<60	35	61	59 (15 %)
$\mathbf{4}^{2+}$	g value	2.433	2.467	2.343	2.378	1.947	1.890
M=Ir	HFI_{Ir} (sd)	82	105	<130	112	120	178 (78 %)
N-ligand=pla	$HFI_{N\text{-amine}}$ (sd)	<60	36	<60	36	60	59 (15 %)
	NQI (η)	−54	−51	−54	−72	+108(0)	+123 (0.17)
$\mathbf{5}^{2+}$	g value	2.244	2.215^T, 2.206	2.204	2.176^T, 2.180	1.992	1.9845^T, 1.985
M=Rh	HFI_{Rh} (sd)	<60	1^T, 6	<60	8^T, 10	60	64 (73 %)^T, 71 (74 %)
N-ligand=Bn-dla	$HFI_{N\text{-amine}}$ (sd)	45.6^a	34^T, 32	41.8^a	34^T, 32	64.4^a (17 %)	64 (18 %)^T, 61 (18 %)
$\mathbf{6}^{2+}$	g value	2.500	2.496^T, 2.470	2.362	2.350^T, 2.364	1.923	1.889^T, 1.891
M=Ir	HFI_{Ir} (sd)	<105	71^T, 82	<90	82^T, 89	108	140 (73 %)^T, 151 (75 %)
N-ligand=Bn-dla	$HFI_{N\text{-amine}}$ (sd)	<40	36^T, 34	<40	36^T, 34	60	64 (17 %)^T, 61 (18 %)
	NQI (η)	−60	-45^T, −45	−60	-73^T, −75	+120(0)	+118 (0.24)^T, +120 (0.25)

[a] η = NQI "rhombicity parameter" $= (Q_1 - Q_2)/Q_3$; nr = not resolved; sd = Mulliken spin density population at the respective atom; ^{T} = structure with twisted N-ligand backbone, see Figure 4; ^{a} = from ENDOR measurements

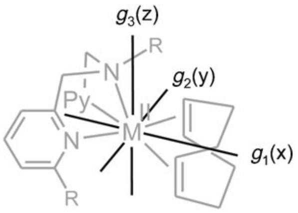

Figure 6. Directions of the principle axes of the g tensor in the molecular axis system of complexes $\mathbf{1}^{2+}$–$\mathbf{6}^{2+}$ as derived from the DFT calculations.

the $g_3(z)$ axis. The other N donors only give rise to marginal HFIs (for all complexes these calculated values vary between 0 and 8 MHz in all directions).

From the experimental anisotropic N_{amine} hyperfine couplings of complex $\mathbf{5}^{2+}$ determined from ENDOR measurements (see Table 5 and Experimental Section) we calculate that the electron resides to about 17 % at the N_{amine} donor (ca. 13.9 % in the 2p orbital and ca. 3.5 % in the 2s orbital),[14] which is in good agreement with the DFT calculations.

Similar large spin populations at N were observed for amine adducts of Rh^{II} porphyrin species $[Rh^{II}(por)(NR_3)]$.[15] Apparently, besides the $M^{II}(NR_3)$ metalloradical description, the $M^I(NR_3^{\bullet+})$ amine radical description seems to be an important resonance structure of amine adducts of Rh^{II} and Ir^{II} species (see Figure 7).

This may seem a strange description, but the only known example of a stable aminyl radical coordinated to a transition metal complex was obtained by one-electron oxidation of a bis-olefin rhodium(I) complex with two pyridyl donors and an amide (NR_2^-) donor (see Scheme 3), a complex very similar to complexes $\mathbf{1}^{2+}$–$\mathbf{6}^{2+}$.[16]

In this case, 56 % of the spin density is located at the amine (aminyl) nitrogen atom and 30 % at the rhodium center. Considering the fact that in our case we are dealing with neutral amines instead of anionic amides, the amount of spin delocalization to the amine nitrogen atom is substantial.

Reactivity of M^{II}(cod) towards dioxygen: Treatment of $\mathbf{1}^{2+}$ with dioxygen in acetone at room temperature, followed by rapid freeze quenching in liquid nitrogen, leads to a different EPR spectrum (Figure 8). The g values of this new species are comparable to those of rhodium superoxo complexes.[17]

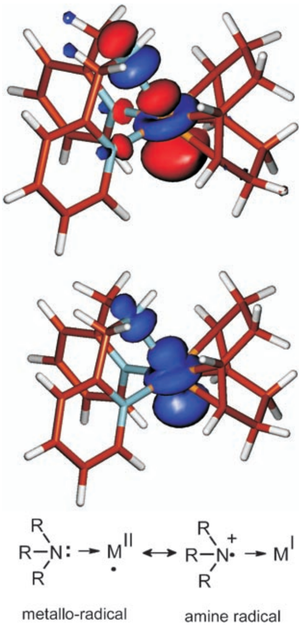

Figure 7. SOMO (top) and spin density plot (middle) of $\mathbf{2}^{2+}$ (Turbomole b3-lyp, TZVP), and the two resonance structures (bottom) describing the electronic structures of $\mathbf{1}^{2+}$–$\mathbf{6}^{2+}$.

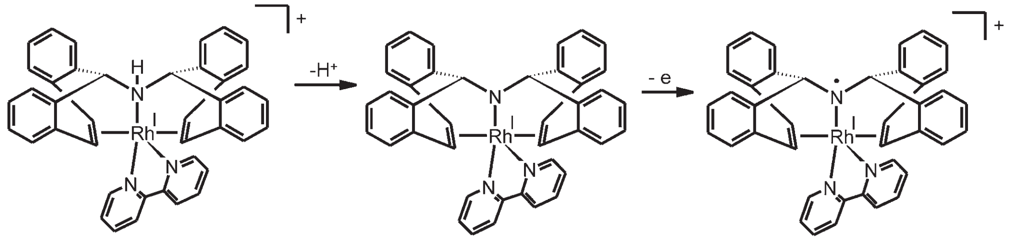

Scheme 3. Formation of stable transition metal coordinated aminyl radical.[16]

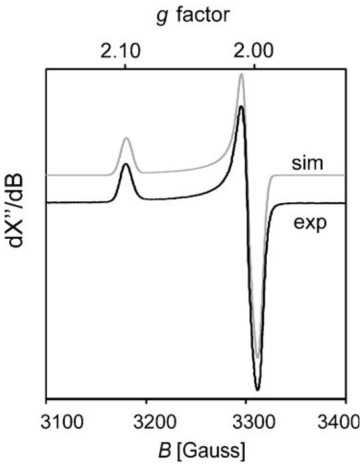

Figure 8. X-band EPR spectrum of superoxide complex $\mathbf{7}^{2+}$ in frozen acetone at 20 K. Conditions: frequency = 9.2999 GHz, mod. amplitude = 4 G, attenuation = 30 dB. The simulation was obtained with the parameters $g_{\parallel} = 2.0891$, $g_{\perp} = 2.0090$, $A_{\perp}^{Rh} = 22$ MHz (not resolved).

This new superoxo complex $\mathbf{7}^{2+}$ is relatively stable and does not react with, for example, dichloromethane. Binding of dioxygen to rhodium(II) does not lead to C–O bond formation between the cod olefin fragments and the superoxo fragment (Scheme 4). Instead, $\mathbf{7}^{2+}$ seems to decompose via $\mathbf{1}^{2+}$ to yield the same mixture of products as obtained from $\mathbf{1}^{2+}$ in absence of dioxygen (see below). This suggests that binding of dioxygen might be reversible.

The Ir^{II} dpa complex $\mathbf{2}^{2+}$ is too reactive to study oxygenation in solution, but $\mathbf{2}^{2+}$ is converted to superoxide $\mathbf{8}^{2+}$ on treatment of powdered solid [**2**]$(PF_6)_2$ with dioxygen. As for the rhodium superoxo complex, no C–O bond formation occurs, and once the mixture is dissolved it rapidly decomposes into the same mixture of products as is observed in the absence of dioxygen (see below). Powdered solid [**1**]$(PF_6)_2$ did not react with O_2.

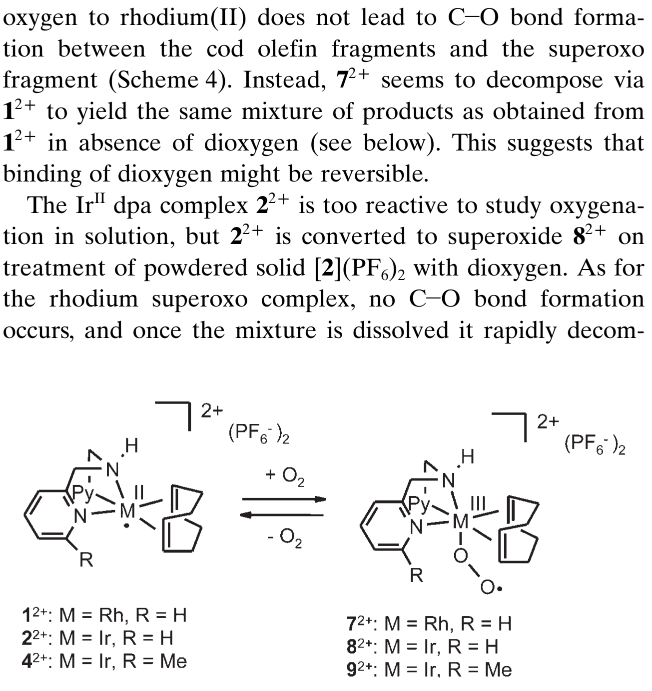

Scheme 4. Reversible binding of dioxygen to $\mathbf{1}^{2+}$, $\mathbf{2}^{2+}$, and $\mathbf{4}^{2+}$.

Species $\mathbf{3}^{2+}$, $\mathbf{5}^{2+}$, and $\mathbf{6}^{2+}$ with sterically demanding dla and Bn-dla ligands did not reveal any formation of a superoxo complex on contact with dioxygen, either as a solid or in solution. Apparently, the bulky methyl groups at the Py-6 position of the ligand shield the M^{II} center from binding O_2. Steric bulk also hinders dioxygen binding to pla-Ir^{II} complex $\mathbf{4}^{2+}$, but for this species we observed formation of a small amount (ca. 0.1–1%) of an iridium(III) superoxide species on contact of an acetone solution with dioxygen. Longer exposure to dioxygen does not affect the iridium(II)/iridium(III) superoxide ratio, and when a stream of nitrogen is passed trough the solution, the EPR signals of the superoxide species disappear ($\mathbf{4}^{2+}$ remains present with unchanged intensity). This is a strong indication that oxygenation of the M^{II} species to M^{III}(superoxo) species is indeed reversible.

As is clear from the above oxygenation experiments, the accessibility of the metal center in $\mathbf{1}^{2+}$–$\mathbf{6}^{2+}$ strongly depends on the steric bulk present at the pyridine 6-position of the N-ligand.

Selective conversion of M^{II}(cod) to M^{III}(allyl) and protonated M^{I}(cod): In acetone, the M^{II}(cod) species $\mathbf{1}^{2+}$–$\mathbf{6}^{2+}$ all transform into two types of diamagnetic complexes at room temperature, albeit with different rates. In case of $\mathbf{1}^{2+}$ 50% is converted to $\mathbf{1H}^{2+}$, and 50% is to two isomers of Rh^{III}(allyl) species $\mathbf{10}^{2+}$ (i.e., $\mathbf{10_A}^{2+}$ and $\mathbf{10_B}^{2+}$ (2:1); Scheme 5). Both $\mathbf{1H}^{2+}$ and $\mathbf{10}^{2+}$ were analyzed by X-ray diffraction (Figure 9, Tables 6 and 7).

Complex $\mathbf{1H}^{2+}$ is a square-planar Rh^{I}(cod) complex in which the dpa ligand is κ^2 coordinated via a N_{Py} and the N_{amine} donor. The other pyridine group is noncoordinating and protonated. In solution $\mathbf{1H}^{2+}$ is in equilibrium with unprotonated $\mathbf{1}^{+}$, which results in broadened NMR signals.

The X-ray structure of $\mathbf{10_A}^{2+}$ reveals a six-coordinate Rh^{III}(allyl) species. The κ^3-dpa ligand is facially coordinated in a distorted octahedral coordination geometry. The three remaining coordination sites are occupied by the olefinic double bond and the allyl moiety of the η^2,η^3-cycloocta-2,5-dien-1-yl fragment (counting the π-η^3-allyl moiety as occupying two coordination sites).

For the two other Rh^{II}(cod) complexes $\mathbf{3}^{2+}$ and $\mathbf{5}^{2+}$ similar 1:1 mixtures of $[Rh^{III}$(cyclooctadienyl)(N-ligand)$]^{2+}$ allyl species ($\mathbf{13}^{2+}$ and $\mathbf{18}^{2+}$, respectively) and $[Rh^{I}$(cod)(N-li-

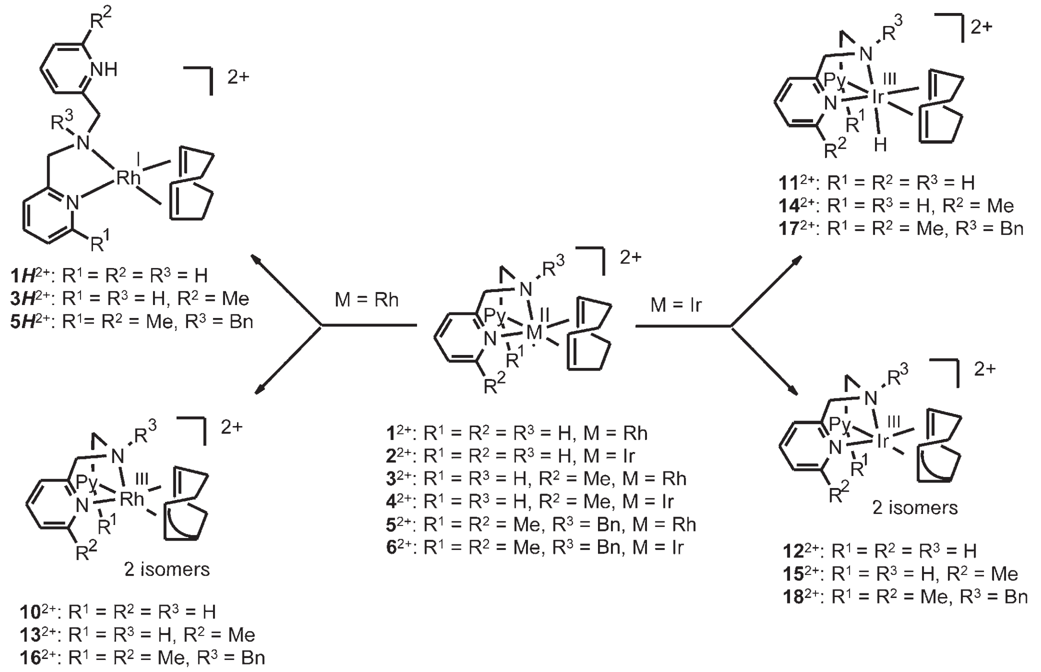

Scheme 5. Conversion of $[M^{II}(cod)(N\text{-}ligand)]^{2+}$ complexes $\mathbf{1}^{2+}$–$\mathbf{6}^{2+}$ to allyl species $[M^{III}(cyclooctadienyl)(N\text{-}ligand)]^{2+}$ (M = Rh, Ir) and equimolar amounts of $[Rh^{I}(cod)(N\text{-}ligandH)]^{2+}$ (for M = Rh) or $[Ir^{III}(H)(cod)(N\text{-}ligand)]^{2+}$ (for M = Ir).

gandH)]$^{2+}$ species ($\mathbf{3H}^{2+}$ and $\mathbf{5H}^{2+}$, respectively) were obtained (see Scheme 5). The Ir^{II}(cod) complexes $\mathbf{2}^{2+}$, $\mathbf{4}^{2+}$, and $\mathbf{6}^{2+}$ also decompose at room temperature in acetone. Similar to rhodium, 50% is converted to $[Ir^{III}(cyclooctadienyl)(N\text{-}ligand)]^{2+}$ allyl species ($\mathbf{12}^{2+}$, $\mathbf{15}^{2+}$, and $\mathbf{18}^{2+}$, respectively). In contrast to rhodium, however, the other 50% ends up as $[Ir^{III}(H)(cod)(N\text{-}ligand)]^{2+}$ hydride species ($\mathbf{11}^{2+}$, $\mathbf{14}^{2+}$, and $\mathbf{17}^{2+}$, respectively) instead of $[M^{I}(cod)(N\text{-}ligandH)]^{2+}$ (see Scheme 5).

We were able to grow crystals of $[Ir^{III}(H)(cod)(dpa)](PF_6)_2$ ($[\mathbf{11}](PF_6)_2$), suitable for X-ray diffraction by overlayering an acetone solution with dioxane. Complex $\mathbf{11}^{2+}$ has an octahedral structure with a facially coordinated dpa ligand. The hydrido ligand occupies the position *trans* to the N_{amine} donor. The remaining two coordination sites are occupied by the cyclooctadiene double bonds (see Figure 9).

The $[Rh^{I}(cod)(N\text{-}ligandH)]^{2+}$ species ($\mathbf{1H}^{2+}$, $\mathbf{3H}^{2+}$ and $\mathbf{5H}^{2+}$), but also the $[Ir^{III}(H)(cod)(N\text{-}ligand)]^{2+}$ hydride species ($\mathbf{11}^{2+}$, $\mathbf{14}^{2+}$, and $\mathbf{17}^{2+}$), can also be obtained by protonation of $[M^{I}(cod)(N\text{-}ligand)]^{+}$ complexes $\mathbf{1}^{+}$–$\mathbf{6}^{+}$. The protonation is reversible, and $\mathbf{1}^{+}$–$\mathbf{6}^{+}$ can be recovered on addition of a base (Na_2CO_3).

Thus, effectively, stoichiometric one-electron oxidation of the M^{I}(cod) complexes followed by decomposition of M^{II}(cod) via the reactions in Scheme 5 yields 50% of M^{III}(allyl) species and 50% protonated M^{I}(cod) starting material. It is therefore not surprising that oxidation of M^{I}(cod) species $\mathbf{1}^{+}$–$\mathbf{6}^{+}$ with an excess of oxidant leads to nearly quantitative formation of the M^{III}(allyl) species $\mathbf{10}^{2+}$, $\mathbf{12}^{2+}$, $\mathbf{13}^{2+}$, $\mathbf{15}^{2+}$, $\mathbf{16}^{2+}$, and $\mathbf{18}^{2+}$.

The rate at which complexes $\mathbf{1}^{2+}$–$\mathbf{6}^{2+}$ decompose is strongly dependent on both the metal and the nature of the N-ligand. The $[M^{II}(cod)(dpa)]^{2+}$ complexes $\mathbf{1}^{2+}$ and $\mathbf{2}^{2+}$ containing the least sterically demanding and most strongly coordinating dpa ligand decompose most rapidly, whereby Ir^{II} complex $\mathbf{2}^{2+}$ decomposes faster than Rh^{II} complex $\mathbf{1}^{2+}$. At room temperature both $\mathbf{1}^{2+}$ and $\mathbf{2}^{2+}$ decompose nearly instantaneously (via the reactions depicted in Scheme 5). At −78 °C, Rh^{II} complex $\mathbf{1}^{2+}$ is still detectable after a few hours and sufficiently long-lived for convenient EPR measurements. Complex $\mathbf{2}^{2+}$ is so reactive that we were unable to detect EPR spectra from frozen solutions, even when the complex was dissolved in acetone at −78 °C and rapidly freeze-quenched in liquid N_2.

On going from the dpa complexes ($\mathbf{1}^{2+}$ and $\mathbf{2}^{2+}$) to the pla complexes ($\mathbf{3}^{2+}$ and $\mathbf{4}^{2+}$), the decomposition rate decreases. The pla complexes can be kept in acetone for 30 s at room temperature before complete decomposition. Apparently, increasing the steric bulk around the metal center by replacing Py by PyMe protects the M^{II}(cod) complexes. Further shielding of the metal by an additional PyMe group further decreases the rate of decomposition.[18] Protection of N_{amine} by introducing an N-benzyl moiety has a further stabilizing effect. The Bn-dla complexes $\mathbf{5}^{2+}$ and $\mathbf{6}^{2+}$ remain intact for several minutes in acetone at room temperature. For the Bn-dla complexes, the difference in stability between Rh^{II} complex $\mathbf{5}^{2+}$ and Ir^{II} complex $\mathbf{6}^{2+}$ is marginal.

As described in the introduction, M^{II}(olefin) species containing allylic hydrogen atoms may have a general tendency to convert to M^{III}(allyl) species (M = Rh, Ir). Two notable

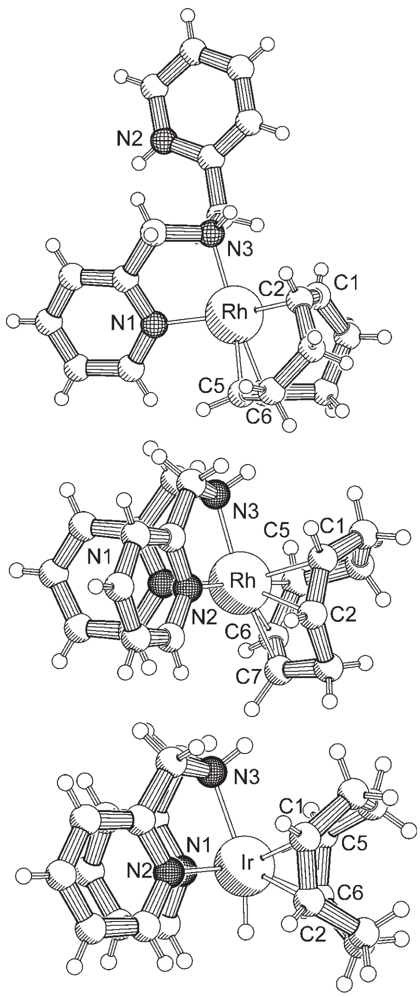

Figure 9. X-ray structures of $\mathbf{1H}^{2+}$ (top), $\mathbf{10}^{2+}$ (middle), and $\mathbf{11}^{2+}$ (bottom).

Table 6. Selected bond lengths [Å] of $\mathbf{1H}^{2+}$, $\mathbf{10}^{2+}$, and $\mathbf{11}^{2+}$.[a]

	[**1H**]$(PF_6)_2$	[**10**]$(PF_6)_2$	[**11**]$(PF_6)_2$
M−N1	2.105(5)	2.104(7)	2.070(2)
M−N2		2.062(6)	2.0705(19)
M−N3	2.135(5)	2.136(6)	2.184(2)
M−C1	2.125(7)	2.236(9)	2.179(2)
M−C2	2.143(8)	2.233(9)	2.197(2)
M−C5	2.135(7)	2.173(9)	2.189(2)
M−C6	2.125(7)	2.148(9)	2.190(2)
M−$X_{1,2}$	2.030	2.133	2.076
M−$X_{5,6}$	2.020	2.049	2.076
M−$X_{6,7}$		2.082	
M−C7		2.245(8)	
C1−C2	1.370(13)	1.331(16)	1.384(4)
C5−C6	1.393(11)	1.370(14)	1.388(4)
C6−C7	1.491(12)	1.400(14)	1.516(4)

[a] $X_{1,2}$ = centroid between C1 and C2; $X_{5,6}$ = centroid between C5 and C6; $X_{6,7}$ = centroid between C6 and C7.

exceptions are $[M^{II}(C_6Cl_5)_2(cod)]$ (M = Rh, Ir) and $[Rh^{II}(\eta^5\text{-}C_5Ph_5)(cod)]^+$, which are reported to be stable at room temperature.[19,20] These species are sterically rather shielded around the metal atom, and this may explain their stability.

Table 7. Selected bond angles [°] of $\mathbf{1H}^{2+}$, $\mathbf{10}^{2+}$, and $\mathbf{11}^{2+}$.[a]

	[**1H**]$(PF_6)_2$	[**10**]$(PF_6)_2$	[**11**]$(PF_6)_2$
N1-M-N2		84.6(3)	85.23(8)
N1-M-N3	79.2(2)	79.0(3)	79.47(8)
N2-M-N3		80.0(3)	78.97(8)
N1-M-C1	163.3(3)	97.6(4)	166.17(9)
N1-M-C2	157.7(3)	86.3(3)	156.93(9)
N1-M-C5	94.9(3)	176.9(3)	97.40(9)
N1-M-C6	99.7(3)	140.6(3)	91.18(9)
N1-M-C7		109.4(3)	
N2-M-C1		165.7(4)	93.41(8)
N2-M-C2		149.3(4)	94.46(9)
N2-M-C5		96.8(4)	165.89(9)
N2-M-C6		86.9(4)	158.13(9)
N2-M-C7		104.8(3)	
N3-M-C1	93.2(3)	86.5(4)	86.76(9)
N3-M-C2	97.2(3)	116.4(4)	123.19(9)
N3-M-C5	161.8(3)	104.0(4)	86.86(9)
N3-M-C6	99.7(3)	136.9(3)	121.61(9)
N3-M-C7		170.5(3)	
C1-M-C2	37.4(4)	34.7(4)	36.87(10)
C1-M-C5	96.6(3)	81.7(4)	80.47(9)
C1-M-C6	82.2(3)	99.8(4)	95.02(10)
C1-M-C7		87.9(4)	
C2-M-C5	81.6(3)	91.5(4)	88.88(9)
C2-M-C6	91.1(3)	88.4(4)	80.54(10)
C2-M-C7		61.1(4)	
C7-M-C5		67.5(4)	
C7-M-C6		37.1(4)	
C5-M-C6	38.1(3)	37.0(4)	36.97(10)
N1-M-$X_{1,2}$	173.67	92.03	175.24
N2-M-$X_{1,2}$	-	175.94	94.15
N3-M-$X_{1,2}$	94.44	101.58	105.07
N1-M-$X_{5,6}$	97.81	159.16	94.52
N2-M-$X_{5,6}$	-	91.98	176.59
N3-M-$X_{5,6}$	177.31	116.36	104.34
N1 M-$X_{6,7}$		125.29	
N2-M-$X_{6,7}$		96.31	
N3-M-$X_{6,7}$		155.27	
$X_{1,2}$-M-$X_{5,6}$	87.84	90.37	85.92
$X_{1,2}$-M-$X_{6,7}$		83.78	

[a] $X_{1,2}$ = centroid between C1 and C2; $X_{5,6}$ = centroid between C5 and C6; $X_{6,7}$ = centroid between C6 and C7.

The general tendency of less hindered M^{II}(olefin) species to decompose via allylic C−H activation was further investigated by looking at the fate of an Ir^{II}(propene) species generated in situ. Indeed, one-electron oxidation of $[Ir^{I}(Me_2tpa)(propene)]^+$ ($\mathbf{19}^+$; for X-ray data, see Supporting Information) with $AgPF_6$ in acetonitrile afforded the Ir^{III}(allyl) species $[Ir^{III}(\eta^3\text{-propenyl})(Me_2tpa)]^{2+}$ ($\mathbf{20}^{2+}$) in about 50% yield (Me_2-tpa = *N*-(2-pyridylmethyl)-*N*,*N*-bis[(6-methyl-2-pyridyl)methyl]amine; see Scheme 6).

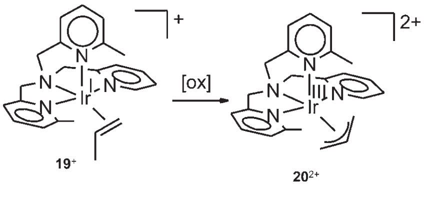

Scheme 6. Allylic hydrogen activation after oxidation of Ir^{I}(propene) complex $\mathbf{19}^+$.

Kinetic studies and mechanistic considerations: At first sight the obtained M^{III}(allyl)- and (protonated) M^{I}(cod)-type products from decomposition of M^{II}(cod) (Scheme 5) suggest a mechanism in which electron transfer (i.e., disproportionation) is followed by deprotonation of the tricationic M^{III}(cod) intermediate. However, the electrochemical data (Table 3) clearly suggest otherwise. Oxidation of the solvent is easier than oxidation of the M^{II} species to their corresponding M^{III} species. In addition, we recently described that very similar $[Rh^{II}$(N-ligand)(nbd)$]^{2+}$ complexes (nbd = norbornadiene, which has much less reactive allylic C−H bonds than cod) are stable towards disproportionation in acetone (in the absence of Cl^- anions).[11] We thus need to consider alternative mechanisms.

Decomposition via ligand aminyl radicals? In a recent paper, Grützmacher and co-workers demonstrated that one-electron oxidation of an Rh^{I}(amido) complex yields a Rh^{I}(aminyl radical) complex instead of the expected Rh^{II}(amido) species (Scheme 3).[16] The thus-obtained rhodium-bound aminyl radical proved to be a potent hydrogen-abstracting radical. Inspired by this work, we argued that deprotonation of the NH moiety of complexes $\mathbf{1}^{2+}$–$\mathbf{4}^{2+}$ might well generate a similar aminyl radical, which in turn should be capable of abstracting an allylic hydrogen atom from another M^{II}(cod) species. At first sight, this seems a plausible mechanism for the decomposition of $\mathbf{1}^{2+}$–$\mathbf{4}^{2+}$ (Scheme 7).

However, DFT calculations suggest that the hypothetical N-deprotonated form of $\mathbf{1}^{2+}$ is better described as a metalloradical rather than a ligand radical. The Mulliken spin population at nitrogen represents only about 30 % of the total spin density, which is substantially lower than in the complex of Grützmacher et al. (56 %). This, in combination with the fact that the amine-protected $\mathbf{5}^{2+}$ and $\mathbf{6}^{2+}$ decompose to give similar species (albeit more slowly), makes the mechanism depicted in Scheme 7 less attractive, but we cannot completely rule out this possibility for $\mathbf{1}^{2+}$–$\mathbf{4}^{2+}$.

Kinetic studies: To obtain more information about the reaction mechanism we followed the kinetics of decomposition of $\mathbf{5}^{2+}$ and $\mathbf{6}^{2+}$ with UV/Vis spectroscopy at their characteristic bands at 680 and 790 nm, respectively (Figure 10). The rate of decay of both $\mathbf{5}^{2+}$ and $\mathbf{6}^{2+}$ proved to be second-order in M^{II}(cod) with observed rate constants k_{obs} of $0.02 \pm 0.02\,L\,mol^{-1}\,s^{-1}$ for $\mathbf{5}^{2+}$ and $0.01 \pm 0.02\,L\,mol^{-1}\,s^{-1}$ for $\mathbf{6}^{2+}$. The considerable spread in absolute k_{obs} values observed for different batches of $\mathbf{5}^{2+}$ and $\mathbf{6}^{2+}$ in neat acetone suggests that impurities play an important role in their rate of decomposition (vide infra). This prevented us from obtaining reliable kinetic isotope effect (KIE) data by comparing the rates for $\mathbf{6}^{2+}$ and its $[D_{12}]$cod[21] analogue $[D_{12}]\mathbf{6}^{2+}$.[22] The spread in the k_{obs} values between different batches also decreases the accuracy of $\Delta S^{\ddagger}$ values from Eyring plots somewhat, but these errors are small enough to obtain useful data. Following the decomposition of $\mathbf{6}^{2+}$ in the temperature range from 288 to 303 K thus yielded the activation parameters $\Delta H^{\ddagger} = 11.5 \pm 2\,kcal\,mol^{-1}$, $\Delta S^{\ddagger} = -27 \pm 10\,cal\,K^{-1}\,mol^{-1}$, and $\Delta G^{\ddagger}_{298\,K} = 19.5 \pm 5\,kcal\,mol^{-1}$ (measurements in triplo). The strongly negative activation entropy is consistent with decomposition via a second-order reaction in the metal.

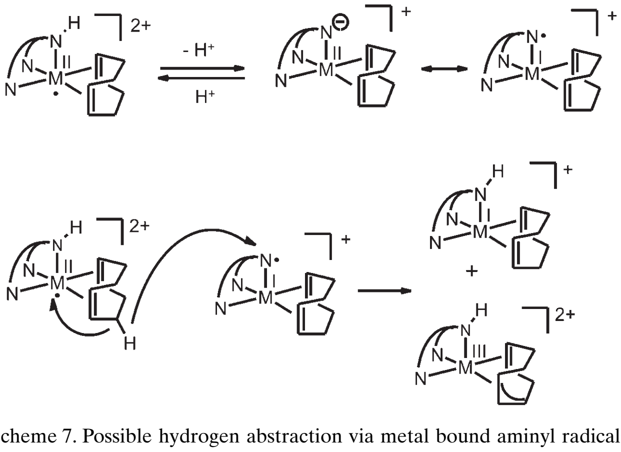

Scheme 7. Possible hydrogen abstraction via metal bound aminyl radicals.

With the deprotonation mechanism in Scheme 7 in mind, we were surprised to find that addition of the acid $[H(OEt_2)_2]B(Ar^F)_4$ ($Ar^F = 3,5\text{-}(CF_3)_2C_6H_3$) clearly accelerates the decomposition of $\mathbf{5}^{2+}$ and $\mathbf{6}^{2+}$. Because decomposition of $\mathbf{6}^{2+}$ is slow enough to follow on convenient timescales, we studied the rate acceleration on addition of varying amounts of $[H(OEt_2)_2]B(Ar^F)_4$ (Figure 10). Plotting k_{obs} (still second-order in $[M^{II}$(cod)$]$) versus $[H^+]$ afforded a straight line. The observed rate constant also increased linearly on addition of coordinating solvents such as MeCN.[22] Clearly, the rate expression is first-order in both $[H^+]$ and [S]. This yields the rate expression $-d[M^{II}]/dt = k_{obs}[M^{II}]^2$ with $k_{obs} = k'[H^+][S]$, where [S] is the concentration of additional coordinating reagents such as MeCN.

The reaction is only first-order in $[H^+]$ at low concentrations. The rate acceleration begins to saturate on addition of more than one equivalent of $[H(OEt_2)_2]B(Ar^F)_4$. The occurrence of H^+ in the rate expressions points to protonation of the dicationic species, most likely at a dissociated pyridine fragment.

Decomposition via metalloradicals: Several metalloradicals are capable of $H^{\bullet}$ abstraction,[2,23] and in a previous communication[7] we already discussed the possibility of hydrogen abstraction from an allylic C−H bond of M^{II}(cod) by the metal center of another M^{II}(cod) fragment as an explanation for the decomposition of $\mathbf{1}^{2+}$ (Scheme 8).

Direct hydrogen abstraction seems quite possible for $\mathbf{1}^{2+}$ and $\mathbf{2}^{2+}$, but CPK models indicate that metal-centered hydrogen-atom abstractions are severely hindered by N-ligand bulk for the complexes $\mathbf{3}^{2+}$–$\mathbf{6}^{2+}$ (Figure 11). This is in agreement with the low tendency of $\mathbf{3}^{2+}$–$\mathbf{6}^{2+}$ to bind dioxygen (see above).

Thus, unless a PyMe donor dissociates from the divalent metal center, a hydrogen-abstraction mechanism involving the metal center seems irrational for these complexes. However, according to DFT calculations dissociation of a pyridyl donor is not a very easy process (Scheme 9). Dissociation of

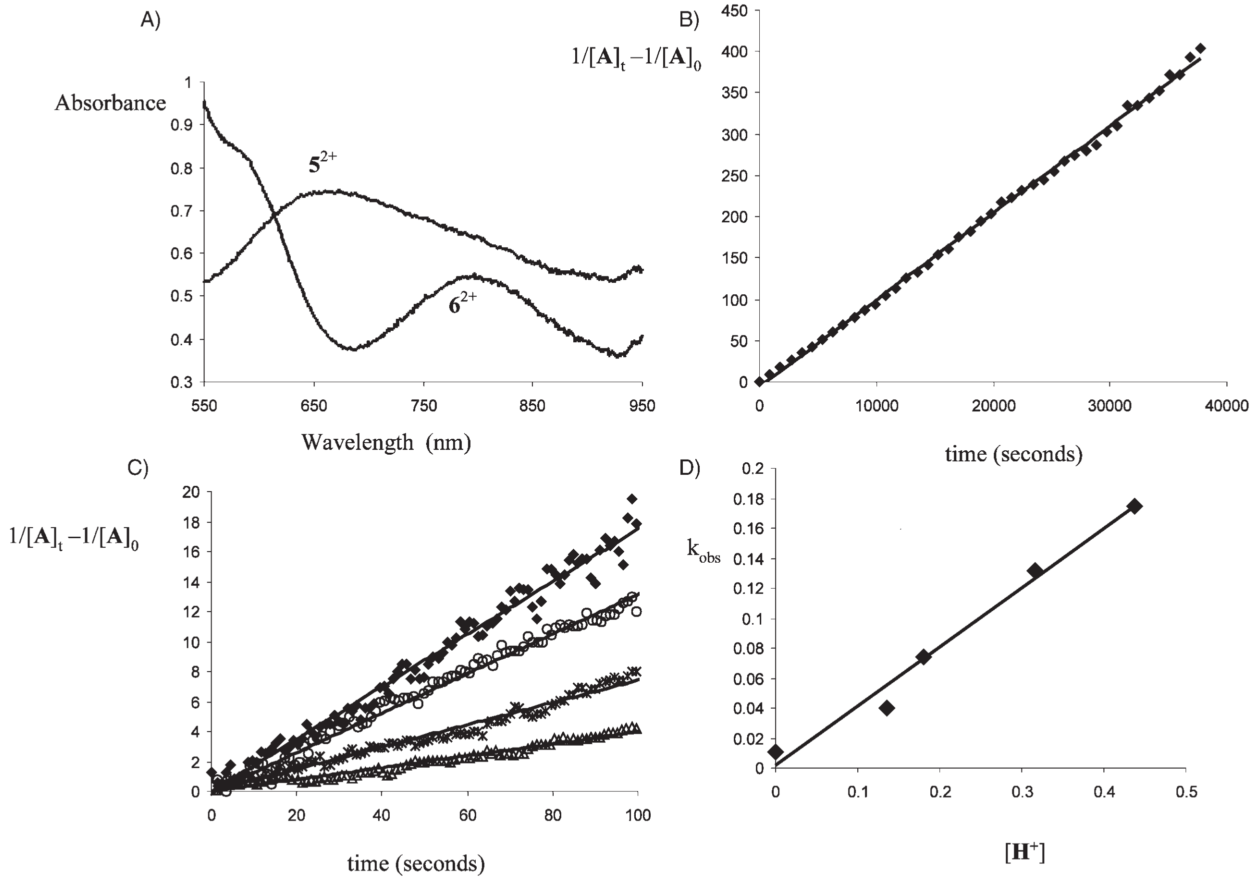

Figure 10. A) Visible part of the UV/Vis spectra of 5^{2+} and 6^{2+}. Plotting $1/[M^{II}(cod)]$ versus time yields straight lines for 5^{2+} (not depicted) and 6^{2+} (B) with k_{obs} of 0.023 and 0.011, respectively. Addition of 0.44 (◆), 0.32 (○), 0.18 (×), and 0.14 (△) equivalents of $[H(OEt_2)_2]B(Ar^F)_4$ increases $k_{obs}(6^{2+})$ significantly (C). Plotting k_{obs} of 6^{2+} versus $[H^+]$ (in equivalents) yields a straight line (D). Plotting k_{obs} of 6^{2+} versus [MeCN] (in equivalents) also yields a straight line (not depicted). $[A]_0$ in all cases was $7.43\times10^{-2}\,mol\,L^{-1}$ (5^{2+}) or $3.28\times10^{-2}\,mol\,L^{-1}$($6^{2+}$). The reaction temperature was maintained at 20°C.

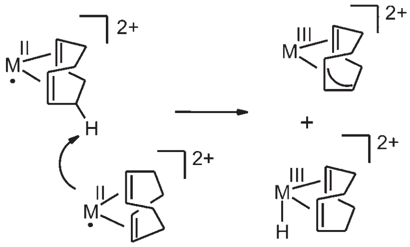

Scheme 8. Direct hydrogen-atom abstraction of an allylic C–H bond of M^{II}(cod) by M^{II}.

a PyMe donor from 3^{2+} and 4^{2+} is easier than dissociation of a Py donor from 1^{2+} or 2^{2+}, and this reflects their relative donor capacities. Surprisingly, however, PyMe dissociation from 5^{2+} and 6^{2+} requires more energy, even more so than Py dissociation from 1^{2+} or 2^{2+}. This likely results from increased steric interactions between the methyl group of the coordinated PyMe fragment and cod on going from five-coordinate 5^{2+} or 6^{2+} to square-planar $5u^{2+}$ or $6u^{2+}$ (Scheme 9).[24] Apart from these differences, direct dissocia-

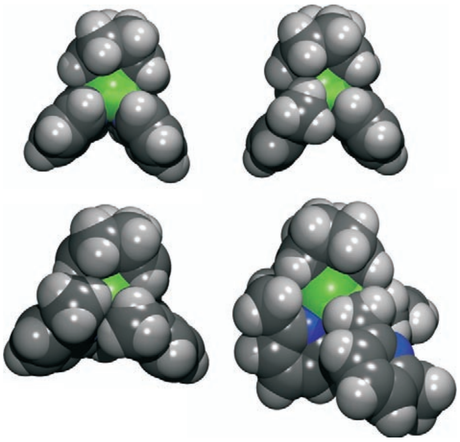

Figure 11. CPK models of 1^{2+} (top, left), 3^{2+} (top, right), and 5^{2+} (bottom, left), showing the two pyridyl fragments and part of the cod ligand wrapped around the M^{II} center and revealing increasing shielding of the metal site. The CPK model of $5u^{2+}$ (bottom, right) is included to show the increased accessibility of the metal center on pyridyl dissociation. The models of 1^{2+}, 3^{2+}, and $5u^{2+}$ are based on the optimized DFT geometries, and that of 5^{2+} is based on the X-ray structure. Drawings were generated with PLATON (rendered with POV-Ray).

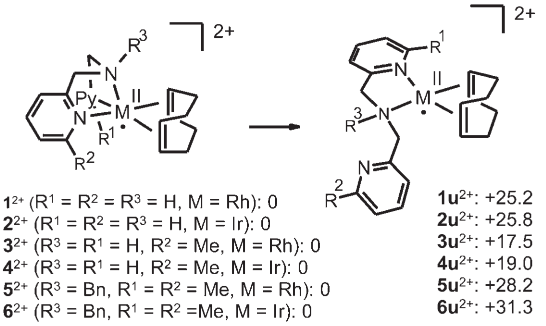

Scheme 9. Energies of the optimized geometries of species obtained after pyridyl dissociation.

tion of a pyridyl donor from the M^{II} sites is substantially endothermic in all cases, which suggests that dissociation of a pyridyl fragment cannot be (entirely) dissociative.[25] It thus seems quite likely that pyridyl dissociation proceeds via a solvent-assisted (or H_2O-assisted) process (Ia or Id mechanism). This also provides a satisfactory explanation for the much faster decomposition rates in (the presence of) MeCN compared to acetone. In absence of MeCN, the coordinating agent is probably H_2O. Indeed, distilling acetone over K_2CO_3[26] prior to use somewhat decreases the observed rate.

For the series **3^{2+}**–**6^{2+}**, it thus seems reasonable to propose that a rate-limiting bimolecular allylic C–H activation process (k) proceeds via a more open M^{II} species formed by dissociation of a PyMe fragment. The concentration of this open species is limited, as determined by the (solvent-dependent) pre-equilibrium (K_{eq}) of PyMe dissociation. The pre-equilibrium is shifted in favor of the open species by subsequent protonation of the dissociated PyMe fragment. This conveniently explains the dependence on H^+. The mechanism proposed in Scheme 10 is in good agreement with the observed rate expression $-d[M^{II}]/dt = k_{obs}[M^{II}]^2$ with $k_{obs} = (k_1 + k_2K_b[H^+])K_{eq}[S]$ (and $K_{eq} \ll K_b$).

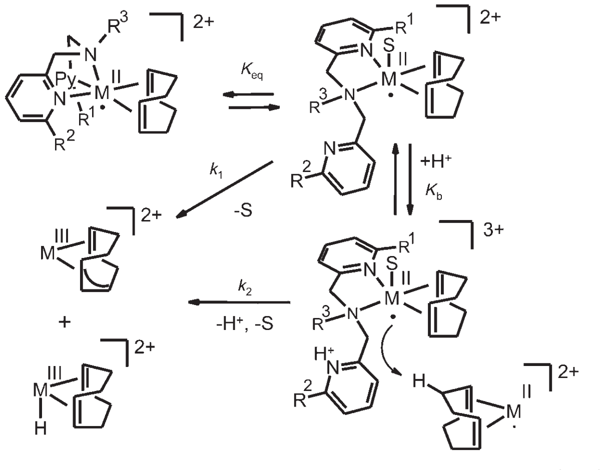

Scheme 10. Proposed mechanism for decomposition of **1^{2+}**–**6^{2+}** (S = solvent) with the theoretical rate expression: $-d[M^{II}]/dt = (k_1 + k_2K_b[H^+])K_{eq}[S][M^{II}]^2$.

Conclusion

Oxidation of $[M^I(cod)(N\text{-ligand})]^+$ complexes (M = Rh, Ir) occurs at relatively low redox potentials and leads to formation of moderately stable M^{II}(cod) species. The 2+ charge prevents direct disproportionation of these species to M^I and M^{III} products. Experimental EPR spectroscopy combined with DFT calculations reveal that the M^{II} species are further stabilized by substantial delocalization of the unpaired spin density over the metal center and the amine nitrogen donor of the ligand.

The $[M^{II}(cod)(N\text{-ligand})]^{2+}$ complexes reversibly bind O_2, but this does not lead to C–O bond formation. Instead, both in the presence and the in absence of O_2, the M^{II}(cod) species transform into a 1:1 mixture of M^{III}(allyl) and (protonated) M^I(cod) species. The decomposition rate strongly depends on the nature of the N-ligand, with slower rates for the sterically more demanding N-donor ligands. The reaction proceeds via a bimolecular pathway and is accelerated by both H^+ and coordinating reagents. The C–H activation process is proposed to proceed via allylic hydrogen-atom abstraction from M^{II}(cod) by another metalloradical. For the more hindered complexes, the C–H activation step is preceded by an initial solvent-assisted pyridyl dissociation step. The Ir^{II}(propene) complex $[Ir^{II}(propene)(Me_2tpa)]^{2+}$ likely decomposes by a similar mechanism to form $[Ir^{III}(allyl)(N\text{-ligand})]^{2+}$.

Experimental Section

General procedures: All procedures were performed under N_2 with standard Schlenk techniques unless indicated otherwise. Solvents were deoxygenated by distillation under N_2 or by the freeze–pump–thaw method. Room temperature (RT) corresponds to about 20 °C. NMR experiments were carried out on a Bruker DPX200 (200 and 50 MHz for ^1H and ^{13}C, respectively) and a Bruker AC300 (300 and 75 MHz for ^1H and ^{13}C, respectively). Solvent references for ^1H spectroscopy: $[D_6]$acetone $\delta_H = 2.05$, $[D_3]$acetonitrile $\delta_H = 1.94$; for ^{13}C NMR: $[D_6]$acetone $\delta_C = 29.50$, $[D_3]$acetonitrile $\delta_C = 1.24$, CD_2Cl_2 $\delta_C = 54.20$. Abbreviations: s = singlet, d = doublet, dd = doublet of doublets, t = triplet, m = multiplet, br = broad, Lu = lutidyl = CH_2PyMe; elemental analyses (CHN) were carried out by the Analytische Laboratorien in Lindlar (Germany). Cyclic voltammetry was performed with an Eco Chemie Autolab PGSTAT20. A conventional three-electrode cell with Pt working and auxiliary electrodes and 0.1 M $[Bu_4N]PF_6$ (TBAH) electrolyte was used. An Ag/AgI reference electrode (grain of AgI, 0.02 M $[Bu_4N]I$ (TBAI), and 0.1 M TBAH) was employed. The complexes $[\{Ir^I(\mu\text{-Cl})(cod)\}_2]$, $[\{Rh^I(\mu\text{-Cl})(cod)\}_2]$, $[\{Ir^I(\mu\text{-Cl})(coe)_2\}_2]$, [**1**]$PF_6$, and [**5**]$PF_6$ and the ligands pla, Bn-dla, and Me_2-tpa were prepared according to literature procedures.[9,11,27] All other chemicals are commercially available and were used without further purification, unless stated otherwise.

EPR and ENDOR spectroscopy: Experimental X-band EPR spectra were recorded on a Bruker ER220 spectrometer. The spectra were simulated by iteration of the anisotropic g values, (super)hyperfine coupling constants, the iridium nuclear quadrupole tensor, and line widths. We thank Dr. F. Neese (MPI Strahlenchemie Mülheim a/d Ruhr) for a copy of his EPR simulation program.

A Q-band pulsed ENDOR spectrum of **5^{2+}** in the range of ^{14}N couplings was recorded on a Bruker Elexsys E-700 FT EPR Q-band spectrometer. The ENDOR spectrum was generated while setting the magnetic field to the maximum intensity position ($g_y = 2.21644$) in the EPR spectrum and performing a Davies pulse ENDOR sequence (t_{180}–t_{RF}–t_{90}–τ–t_{90}–τ–echo) with $t_{RF}=30$ µs, $t_{180}=100$ ns, $t_{90}=50$ ns, $\tau=300$ ns. While monitoring the electron spin echo intensity, the RF frequency (300 W) was scanned in the range in which the ^{14}N transitions were expected. A doublet of doublets was observed (Figure 12). The frequency positions are given by $\nu=(A/2\pm\nu_I)\pm P/2$. This means that the center of the multiplet is positioned at $A/2$ (half the hyperfine splitting), while the major splitting is given by twice the nuclear Larmor frequency (ν_I). The additional splitting is caused by the nuclear quadrupole interaction. The spectrum was simulated with the following parameters: $g=[2.2474, 2.21644, 1.99793]$, $A(^{14}N)=[41.6, 41.6, 64.4]$ MHz. The quadrupole parameters are characterized by $K=0.8$ MHz, $\eta=0$, assuming an axial NQI tensor lying along the molecular z axis.

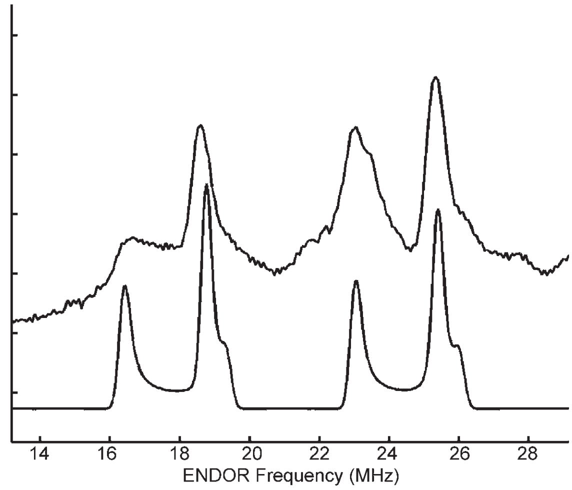

Figure 12. Q-band pulsed ENDOR spectrum of $\mathbf{5}^{2+}$ in the range of ^{14}N couplings. Experimental conditions: $B=10800$ G, microwave frequency = 33.494815 GHz, $T=10$ K.

X-ray diffraction: The structures of $\mathbf{2}^+$, $\mathbf{6_A}^+$, $\mathbf{5_A}^+$, $\mathbf{5}^{2+}$, $\mathbf{1H}^{2+}$, $\mathbf{10}^{2+}$, and $\mathbf{11}^{2+}$ are shown in Figures 2, 3, and 9. All other structures are shown in the Supporting Information. Drawings were generated with the program PLATON.[28] Selected bond lengths and angles are given in Tables 1, 6, and 7. Other relevant structural data are summarized in Table 2. The structures were solved by the program system DIRDIF[29] using the program PATTY[30] to locate the heavy atoms. All non-hydrogen atoms were refined with standard methods (refinement against F^2 of all reflections with SHELXL-97[31]) with anisotropic parameters for the non-hydrogen atoms. The hydrogen atoms were placed at calculated positions and refined isotropically in riding mode. Unless stated otherwise, geometrical calculations[28] revealed neither unusual geometric features nor unusual short intermolecular contacts. The calculations revealed no higher symmetry and no (further) solvent-accessible areas.

[5]$^{2+}$(PF$_6$)$_2$: There is a void in the structure of 295 Å^3 containing, according to the SOLVE procedure of PLATON,[28] 42 electrons. Based on these data and the synthetic route this void probably contains a very disordered diethyl ether solvent molecule. We used the SQUEEZE procedure of PLATON to correct for this electron density. The presence of the diethyl ether molecule was taken into account while calculating the physical properties of the compound.

[1H]$^{2+}$(PF$_6$)$_2$: The assignment of the N2 and C23 atoms is rather tentative. There is no real difference in geometry for these two atoms, and no hydrogen atom could be found in the difference Fourier map for either of them. The assignment is based on the thermal displacement parameters, which seem more in line with neighboring atoms for this assignment, and is supported by ^{1}H NMR spectroscopy. The assignment of CH_2Cl_2 as the solvent molecule is based on the synthetic route. There is some disorder in the PF$_6$ and CH_2Cl_2 moieties, but this could not be described properly by splitting up the atoms. The empirical absorption correction using psi scans proved to be inadequate; therefore, the DIFABS procedure was used.

[10]$^{2+}$(PF$_6$): There is some disorder in the PF$_6$ and 1,4-dioxane moieties, but this could not be described adequately by splitting up the atoms. The assignment of the solvent molecule as 1,4-dioxane was based on the synthetic route.

[11]$^{2+}$(PF$_6$)$_2$: The assignment of the atomic species in the 1,4-dioxane moiety is based on the synthetic route, bond lengths, refinement of occupation factors, and indications in the difference Fourier map for hydrogen atoms near the carbon atoms. The assignment of hydrogen atom H1A is speculative on basis of X-ray diffraction alone, but is supported by ^{1}H NMR spectroscopy.

DFT geometry optimizations and EPR parameter calculations: All geometry optimizations were carried out with the Turbomole program[32a] coupled to the PQS Baker optimizer.[33] Geometries were fully optimized as minima at the BP86[34] level using the Turbomole SV(P) basis set[32c,d] on all atoms (small-core pseudopotential[32c,e] on Rh or Ir). Improved energies were obtained from single-point calculations at the b3-lyp level[35] using the TZVP basis[32c,f] (small-core pseudopotential[32c,e] on Rh or Ir). EPR parameters[36] were calculated with the ADF[37] program system using the BP86[34] functional with the ZORA/TZP basis sets supplied with the program (all-electron, core double-zeta, valence triple-zeta polarized basis set on all atoms) by using the coordinates from the structures optimized in Turbomole as input.

Synthesis of [Ir^{I}(cod)(dpa)]$^+$ (2$^+$):, A slight excess of dpa (70 mg, 0.35 mmol) was added to a suspension of [{Ir^{I}(µ-Cl)(cod)}$_2$] (110 mg, 0.16 mmol) in MeOH (10 mL), and stirred for five minutes at RT. After addition of KPF$_6$ (500 mg) and vigorous stirring for a further 5 min a yellow precipitate of [**2**]PF$_6$ was formed. The precipitate was collected by filtration, washed with a small amount of cold methanol, and dried in vacuo. [**2**]BPh$_4$ was obtained in a similar manner by using NaBPh$_4$ instead of KPF$_6$.

^{1}H NMR (200 MHz, CD_2Cl_2, 298 K): $\delta=8.92$ (d, 2H, $^3J_{H,H}=5.3$ Hz, Py-H6), 7.68 (dt, 2H, $^3J_{H,H}=7.7$ Hz, $^4J_{H,H}=1.3$ Hz, Py-H4), 7.32 (d, 2H, $^3J_{H,H}=5.9$ Hz, Py-H3), 7.19 (t, 2H, $^3J_{H,H}=6.4$ Hz, Py-H5), 5.35 (brs, 1H, NH), 4.78 (dd[AB], 2H, $^2J_{H,H}=17$ Hz, $^3J_{H,H}=7$ Hz, NCH$_2$), 4.28 (d[AB], 2H, $^2J_{H,H}=17$ Hz, NCH$_2$), 3.26 (brd, 4H, CH=CH), 2.33 (brm, 4H, C=CCH$_2$-*exo*), 1.65 ppm (dd, 4H, $^2J_{H,H}=16$ Hz, $^3J_{H,H}=8$ Hz, C=CCH$_2$-*endo*); ^{13}C NMR (75 MHz, CD_2Cl_2, 298 K): $\delta=161.0$ (Py-C2), 151.0 (Py-C6), 138.9 (Py-C4), 125.6 (Py-C5), 123.5 (Py-C3), 61.7 (NCH$_2$), 56.6 (C=C), 33.3 ppm (C=CCH$_2$); FAB$^+$-MS: m/z: 516 $[M+O]^+$, 500 $[M]^+$, 407 $[M-CH_2Py-H]^+$; elemental analysis calcd (%) for [**2**]BPh$_4$ ($C_{44}H_{45}N_3IrB$): C 64.54, H 5.54, N 5.13; found: C 64.69, H 5.54, N 5.20.

Synthesis of [Rh^{I}(cod)(pla)]$^+$ (3$^+$): pla (173 mg, 0.81 mmol) was added to a suspension of [{Rh^{I}(µ-Cl)(cod)}$_2$] (200 mg, 0.81 mmol) in methanol (10 mL). The resulting solution was stirred for an additional 5 min and then an excess of KPF$_6$ was added to precipitate [**3**]PF$_6$. Subsequently, demineralized water (5 mL) was added to cause further precipitation of [**3**]PF$_6$. The reaction mixture was filtered, and the yellow residue washed with a small amount of cold methanol and cold diethyl ether. [**3**]BPh$_4$ was obtained in a similar manner by using NaBPh$_4$ instead of KPF$_6$.

^{1}H NMR (200 MHz, CD_2Cl_2, 298 K): $\delta=8.27$ (d, 1H, $^3J_{H,H}=5.5$ Hz, Py-H6), 7.60 (dt, 1H, $^3J_{H,H}=7.5$ Hz, $^4J_{H,H}=1.6$ Hz, Py-H4), 7.53 (t, 1H, $^3J_{H,H}=7.7$ Hz, Lu-H4), 7.19 (m, 3H, Lu-H5, Lu-H3 and Py-H5), 7.03 (d, 1H, $^3J_{H,H}=7.8$ Hz, Py-H3), 5.05 (m, 2H, NH, NCH$_2$), 4.30 (dd[AB], 1H, $^2J_{H,H}=16.5$ Hz, $^3J_{H,H}=5.8$ Hz, NCH$_2$), 4.04 (dd[AB], 1H, $^2J_{H,H}=19.9$ Hz, $^3J_{H,H}=4.7$ Hz, NCH$_2$), 3.81 (brt, 2H, $^3J_{H,H}=7.0$ Hz, CH=CH), 3.60 (dt, 2H, $^3J_{H,H}=7.0$ Hz, HC=CH), 3.34 (s, 3H, Lu-CH$_3$), 2.8–2.4 (brm, 4H, C=CCH$_2$-*exo*), 2.1–1.7 ppm (brm, 4H, C=CCH$_2$-*endo*); ^{13}C NMR (75 MHz, CD_2Cl_2, 298 K): $\delta=162.7$ (Lu-C6), 160.3 (Py-C2), 156.9 (Lu-C2), 149.3 (Py-C6), 139.1, 138.5 (Lu-C4, Py-C4), 124.9, 124.7 (Lu-C5, Py-C5), 123.02 (Py-C3), 120.9 (Lu-C3), 75.9 ($^1J_{Rh,C}=13.9$ Hz, C=C), 74.6 ($^1J_{Rh,C}=12.5$ Hz, C=C), 61.7 (NCH$_2$), 31.3 (C=CCH$_2$), 28.1 ppm (Lu-CH$_3$); FAB$^+$-MS: m/z: 440 $[M+O]^+$, 424 $[M]^+$, 316 $[M-\text{cod}]^+$; elemental analysis calcd (%) for [**3**](BPh)$_4$ ($C_{45}H_{47}N_3RhB$): C 72.69, H 6.37, N 5.65; found: C 72.98, H 6.47, N 5.79.

Synthesis of [Ir^{I}(cod)(pla)]$^{+}$ (4^{+}): The salts [**4**]PF$_6$ and [**4**]BPh$_4$ were obtained in a similar way to that described for [**2**]PF$_6$ and [**2**]BPh$_4$ by using pla instead of dpa as ligand.

^{1}H NMR (200 MHz, CD$_2$Cl$_2$, 298 K): δ=8.54 (d, 1H, $^3J_{H,H}$=6.4 Hz, Py-H6), 7.70 (dt, 1H, $^3J_{H,H}$=7.7 Hz, $^4J_{H,H}$=1.5 Hz, Py-H4), 7.57 (t, 1H, $^3J_{H,H}$=7.7 Hz, Lu-H4), 7.35 (d, 1H, $^3J_{H,H}$=8.1 Hz, Py-H3), 7.18 (m, 3H, Lu-H5, Lu-H3, and Py-H5), 5.43 (brs, 1H, NH), 5.03 (dd[AB], 1H, $^2J_{H,H}$=17 Hz, $^3J_{H,H}$=7.6 Hz, NCH$_2$), 4.48 and 4.46 (2s, 2H, NCH$_2$), 4.24 (d[AB], 1H, $^2J_{H,H}$=17 Hz, NCH$_2$), 3.30 (s, 3H, Lu-CH$_3$), 3.30 (dt, 2H, CH=CH), 3.08 (dt, 2H, $^3J_{H,H}$=8.1 Hz, $^3J_{H,H}$=2.9 Hz, CH=CH), 2.7–2.1 (brm, 4H, C=CCH$_2$-*exo*), 1.75–1.45 ppm (brm, 4H, C=CCH$_2$-*endo*); ^{13}C NMR (75 MHz, CD$_2$Cl$_2$, 298 K): δ=163.6 (Lu-C6), 160.6 (Py-C2), 158.6 (Lu-C2), 148.7 (Py-C6), 138.8, 138.5 (Lu-C4, Py-C4), 125.2, 124.9 (Lu-C5, Py-C5), 123.0 (Py-C3), 120.7 (Lu-C3), 61.7 (NCH$_2$), 56.9 (C=C), 55.5 (C=C), 33.3 (C=CCH$_2$), 32.5 (C=CCH$_2$), 29.4 ppm (Lu-CH$_3$); FAB$^+$-MS: *m*/*z*: 530 [*M*]$^+$, 514 [*M*−CH$_3$−H]$^+$; elemental analysis calcd (%) for [**4**]BPh$_4$ (C$_{45}$H$_{47}$N$_3$IrB): C 64.89, H 5.69, N 5.04; found: C 65.09, H 5.10, N 4.78.

Synthesis of [Ir^{I}(cod)(Bn-dla)]$^{+}$ (6^{+}): A slight excess of Bn-dla (128 mg, 0.44 mmol) was added to a suspension of [{Ir^{I}(μ-Cl)(cod)}$_2$] (136 mg, 0.20 mmol) in methanol (10 mL) and stirred for 5 min at RT. After addition of KPF$_6$ (500 mg) and 4 mL of dioxygen-free water a yellow precipitate of [**6**]PF$_6$ formed. The precipitate was collected by filtration, washed with a small amount of cold methanol, and dried in vacuo. X-ray-quality crystals were obtained from a saturated acetone solution of [**6**]PF$_6$ at 5 °C.

^{1}H NMR (300 MHz, CD$_2$Cl$_2$, 298 K): δ=7.71 (t, 2H, $^3J_{H,H}$=7.7 Hz, Lu-H4), 7.6–7.5 (5H, Ph), 7.38 (d, 2H, $^3J_{H,H}$=7.7 Hz, Lu-H5), 7.20 (d, 2H, $^3J_{H,H}$=7.6 Hz, Lu-H3), 4.78 (s, 2H, NCH$_2$Ph), 4.72 (d[AB], 2H, $^2J_{H,H}$=15.6 Hz, NCH$_2$), 3.61 (d[AB], 2H, $^2J_{H,H}$=15.5 Hz, NCH$_2$), 3.38 (brs, 2H, CH=CH), 3.34 (s, 6H, Lu-CH$_3$), 2.58 (brs, 2H, CH=CH and 2H, C=CCH$_2$-*exo*), 2.30 (brs, 2H, C=CCH$_2$-*exo*), 1.57 (brs, 2H, C=CCH$_2$-*endo*), 1.43 ppm (brs, 2H, C=CCH$_2$-*endo*); ^{13}C NMR (75 MHz, CD$_2$Cl$_2$, 298 K): δ=162.1 (Lu-C6), 160.4 (Lu-C2), 139.1 (Lu-C4), 132.6 (Bn-C1), 131.8 (Bn-C2/6), 130.1, 130.0 (Bn-C3/5 and Bn-C4), 127.4 (Lu-C5), 122.0 (Lu-C3), 63.1 (Ph-NCH$_2$), 60.8 (Lu-NCH$_2$), 30.1 ppm (Lu-CH$_3$); FAB+-MS: *m*/*z*: 763 [*M*+PF$_6$]$^+$, 618 [*M*]$^+$, 510 [*M*−cod]$^+$, 418 [*M*−CH$_2$Ph−cod]$^+$; elemental analysis calcd (%) for C$_{29}$H$_{35}$N$_3$IrPF$_6$·acetone: C 48.82, H 5.03, N 5.12; found C 46.64, H 4.66, N 5.16.

Synthesis of [Rh^{II}(cod)(dpa)]$^{2+}$ (1^{2+}): [Fc$^+$]PF$_6$ (225 mg, 0.8 equiv) was added to [**1**]PF$_6$ (500 mg) in dichloromethane (50 mL). The solution was stirred for 24 h to give a dark green precipitate of [**1**](PF$_6$)$_2$, which was collected by filtration and subsequently washed with dichloromethane. [**1**](PF$_6$)$_2$·CH$_2$Cl$_2$ was obtained in 82 % yield (580 mg).

μ_{eff}=1.96 μ$_B$; ESI$^+$-MS (acetone): *m*/z: 204.5 [**10**]$^{2+}$, 233.5 [**10**+acetone]$^{2+}$, 410 [**10**]$^+$, 554 [**10**+PF$_6$]$^{2+}$; elemental analysis calcd (%) for C$_{20}$H$_{25}$N$_3$RhP$_2$F$_{12}$·CH$_2$Cl$_2$: C 32.12, H 3.46, N 5.35; Found C 32.31, H 3.41, N 5.51; EPR data of [**1**](PF$_6$)$_2$ are listed in Table 4.

Synthesis of [Ir^{II}(cod)(dpa)]$^{2+}$ (2^{2+}): [**2**]PF$_6$ (400 mg) and [Fc]PF$_6$ (150 mg) were dissolved in dichloromethane (10 mL) and stirred overnight. The mixture was filtered, and the residue washed with dichloromethane and dried in vacuo to yield 330 mg of [**2**](PF$_6$)$_2$ as a red-gray solid (67 % yield).

μ_{eff}=1.5 μ$_B$; ESI$^+$-MS (acetone): *m*/*z* 249.5 [**12**]$^{2+}$, 250.5 [**11**]$^{2+}$, 278.5 [**12**+acetone]$^{2+}$, 279.5 [**11**+acetone]$^{2+}$, 307.5 [**12**+acetone]$^{2+}$, 308.5 [**11**+acetone]$^{2+}$, 500 [**2**]$^+$, 516 [**2**+O]$^+$, 532 [**2**+2O]$^+$, 644 [**12**+PF$_6$]$^+$, [**11**+PF$_6$]$^+$; elemental analysis calcd (%) for C$_{20}$H$_{25}$N$_3$IrP$_2$F$_{12}$.CH$_2$Cl$_2$: C 28.84, H 3.11, N 4.80; Found C 28.71, H 3.28, N 5.05; EPR data of [**2**](PF$_6$)$_2$ are shown in Table 4.

Synthesis of [Rh^{II}(cod)(pla)]$^{2+}$ (3^{2+}): [**3**]PF$_6$ (100 mg) and [Ag]PF$_6$ (70 mg) were dissolved in acetone and stirred for 10 min. The mixture was filtered, and the residue washed with dichloromethane and dried in vacuo to yield 112 mg of [**3**](PF$_6$)$_2$ as a dark green solid (90 % yield). EPR data of [**3**](PF$_6$)$_2$ are listed in Table 5.

Synthesis of [Ir^{II}(cod)(pla)]$^{2+}$ (4^{2+}): [**4**]PF$_6$ (200 mg) and [Fc$^+$]PF$_6$ (90 mg) were dissolved in 6 mL of dichloromethane. The mixture was stirred overnight and filtered, the residue washed with dichloromethane and dried in vacuo, yielding 206 mg of [**4**](PF$_6$)$_2$ as a gray solid (85 % yield).

μ_{eff}=2.1 μ$_B$; ESI$^+$-MS (acetone): *m*/*z* 256.5 [**15**]$^{2+}$, 257 [**4**]$^{2+}$ 257.5 [**14**]$^{2+}$, 285.5 [**15**+acetone]$^{2+}$, 286 [**4**+acetone]$^{2+}$, 286.5 [1**4**+acetone], 514 [**4**]$^+$, 530 [**4**+O]$^+$, 546 [**4**+2O]$^+$; elemental analysis calcd (%) for C$_{21}$H$_{27}$N$_3$IrP$_2$F$_{12}$.CH$_2$Cl$_2$: C 31.39, H 3.39, N 5.41; found C 31.25, H 3.50, N 5.41; EPR data of [**4**](PF$_6$)$_2$ are shown in Table 5.

Synthesis of [Rh^{II}(cod)(Bn-dla)]$^{2+}$ (5^{2+}): [**5**]PF$_6$ (200 mg) and [Ag]PF$_6$ (125 mg) were stirred for half an hour in 3 mL of dichloromethane. The mixture was filtered, and the residue washed with dichloromethane and dried in vacuo yielding a crude mixture containing [**5**](PF$_6$)$_2$ in 75 % yield. The crude mixture was recrystallized from acetone/diethyl ether to give [**5**](PF$_6$)$_2$ as dark green crystals which were suitable for X-ray diffraction. μ_{eff}=1.6 μ$_B$; EPR data of [**5**](PF$_6$)$_2$ are shown in Table 5.

Synthesis of [Ir^{II}(cod)(Bn-dla)]$^{2+}$ (6^{2+}): [Ag]PF$_6$ was added to a solution of [**6**]PF$_6$ in acetone to yield a dark red-purple solution containing **6**$^{2+}$. The mixture was filtered and subsequently evaporated to yield **6**$^{2+}$ as a red solid. EPR data of [**6**](PF$_6$)$_2$ are shown in Table 5.

Decomposition of 1^{2+}: [**1**](PF$_6$)$_2$ was dissolved in acetone. A direct color change from green to yellow was observed, and 50 % **1H**$^{2+}$ and 50 % **10**$^{2+}$ (as a 1:1 mixture of isomers **10$_A$**$^{2+}$ and **10$_B$**$^{2+}$) were obtained.

10$_A$$^{2+}$: ^{1}H NMR (500 MHz, [D$_6$]acetone, 298 K): δ=9.63 (d, $^3J_{H,H}$=5.5 Hz, 1H, Py-H6), 8.55 (d, $^3J_{H,H}$=5.7 Hz, 1H, Py′-*H*6), 7.54 (m, 2H, Py-H5, Py′-*H*5), 7.96 (m, 2H, Py-H4, Py′-H4), 7.68 (m, 2H, Py-H3, Py′-H3), 5.71 (dd[A,B], $^3J_{NH,H}$=5.9 Hz, $^2J_{H,H}$=17.0 Hz, 2H, C*H*$_2$NH), 5.44 (m, 2H, C1H, C2H), 5.17 (m, 1H, C6H), 5.06 (m, 1H, C4H), 5.03 (d, $^2J_{H,H}$=16.9 Hz, C*H*$_2$NH), 4.41 (m, 1H, C5H), 3.91 (m, 1H, C8H), 3.27 (m, 1H, C3H), 3.10 (m, 1H, C8H), 2.53 (m, 1H, C7H), 2.40 (m, 1H, C3H), 2.10 ppm (m, 1H, C7H); ^{13}C NMR (125 MHz, [D$_6$]acetone, 298 K): δ=152.7 (Py-C2), 152.3 (Py′-C2), 145.8 (Py-C6), 142.4 (Py′-C6), 132.7 (Py-C4), 132.2 (Py′-C4), 120.3 (Py-C5), 118.8 (Py-C2), 118.3 (Py′-C2), 116.4 (Py′-C5), 98.9 (C6), 98.4 (C4), 94.4 (CH$_2$NH), 89.9 (C5), 66.5 (C1), 65.3 (C2), 23.8 (C7), 22.4 (C3), 11.8 ppm (C8). Assignment of the NMR signals follows the numbering scheme in Figure 9; elemental analysis calcd (%) for C$_{20}$H$_{24}$N$_3$RhP$_3$F$_{12}$·C$_4$H$_8$O$_2$: C 34.25, H 3.74, N 5.99; found: C 34.15, H 3.62, N 5.80.

Decomposition of 2^{2+}: [**2**](PF$_6$)$_2$ was dissolved in acetone, yielding instantly a yellow solution containing 50 % **11**$^{2+}$ and 50 % **12**$^{2+}$ (as a 2:1 mixture of isomers **12$_A$**$^{2+}$ and **12$_B$**$^{2+}$).

11^{2+}: ^{1}H NMR (500 MHz, [D$_6$]acetone, 298 K): δ=9.41 (d, $^3J_{H,H}$=6.0 Hz, 2H, Py-H6), 8.05 (dt, $^3J_{H,H}$=7.9 Hz, $^4J_{H,H}$=1.5 Hz, 2H, Py-H4), 7.76 (d, $^3J_{H,H}$=8.0 Hz, 2H, Py-H3), 7.51 (t, $^3J_{H,H}$=6. 6 Hz, 2H, Py-H5), 5.70 (dd[A,B], $^3J_{(NH,H)}$=7.0 Hz, $^2J_{H,H}$=18.0 Hz, 2H, C*H*$_2$NH), 5.23 (d, $^3J_{H,H}$=19.0 Hz, 2H, C*H*$_2$NH), 5.18 (m, 2H, CH=CH), 4.86 (m, 2H, 1-C*H*=CH), 3.06 (m, 2H, CH=CHC*H*$_2$-*exo*), 2.93 (m, 2H, CH=CHC*H*$_2$-*exo*), 2.69 (m, 2H, CH=CHC*H*$_2$-*endo*), 2.28 (m, 2H, CH=CHC*H*$_2$-*endo*), −10.98 ppm (s, 1H, IrH); ^{13}C NMR (125 MHz, [D$_6$]acetone, 298 K): δ=160.4 (Py-C2), 153.9 (Py-C6), 140.4 (Py-C4), 127.0 (Py-C5), 123.9 (Py-C3), 88.4 (C=C), 77.3 (C=C), 56.3 (CH$_2$NH), 32.3 (C=C*C*H$_2$). The other C=C*C*H$_2$ signal overlaps with the acetone signal and could not be assigned.

12$_A$ $^{2+}$: ^{1}H NMR (200 MHz, [D$_6$]acetone, 298 K): δ=9.73 (d, $^3J_{H,H}$=5.4 Hz, 1H, Py-H6), 8.60 (d, $^3J_{H,H}$=6.3 Hz, 1H, Py-H6′), 8.04 (m, 2H, Py-H4, Py-H4′), 7.77 (m, 2H, Py-H3, Py-H3′), 7.52 (m, 2H, Py-H5, Py-H5′), 5.80 (m, 2H, C*H*$_2$NH), 5.60–5.35 (m, 2H, C1H, C2H), 5.30–4.97 (m, 4H, C*H*$_2$NH, C4H, C6H), 4.46 (m, 1H, C5H), 4.04 (m, 1H, C8H), 3.38 (m, 1H, C3H), 3,20–2.78 (m, 1H, C8H), 2.65–2.30 ppm (m, 2H, C7H, C3H). The second C7H signal overlaps with the acetone signal and could not be interpreted. ^{13}C NMR (125 MHz, [D$_6$]acetone, 298 K): δ=160.5 (Py-C2), 159.6 (Py-C2), 153.5 (Py-C6), 149.2 (Py-C6), 140.8 (Py-C4), 140.4 (Py-C4), 126.5 (Py-C5), 126.3 (Py-C5), 123.9 (Py-C3), 122.9 (Py-C3), 99.2 (C6), 99.1 (C4), 87.9 (C5), 65.7 (C1), 62.9 ppm (C2). The rest of the ^{13}C signals could not be assigned due to overlapping signals of **12$_A$**$^{2+}$, acetone, and **11**$^{2+}$.

Decomposition of 3^{2+}: Complex **3**$^{2+}$ was generated in situ by dissolving [**3**]PF$_6$ and one equivalent of [Ag]PF$_6$ in acetone. A direct color change to green was observed almost immediately, followed by a color change to yellow after a few minutes with formation of 50 % **3H**$^{2+}$ and 50 % **13**$^{2+}$, with **13**$_{\rm A}^{2+}$ being the major isomer (>60%) among several isomers of **13**$^{2+}$. Full conversion to **13**$^{2+}$ was observed when two or more equivalents of [Ag]PF$_6$ were used.

13$_{\rm A}^{2+}$: ^{1}H NMR (300 MHz, [D$_6$]acetone, 298 K): δ=8.52 (d, $^3J_{\rm H,H}$=5.1 Hz, 1H, Py-H6), 7.89 (dt, $^3J_{\rm H,H}$=5.1 Hz, $^4J_{\rm H,H}$=7.8 Hz, 1H, Py-H4), 7.76 (t, $^3J_{\rm H,H}$=7.8 Hz, 1H, Lu-*H4*), 7.58 (d, $^3J_{\rm H,H}$=7.8 Hz, 1H, Py-H3, or Lu-H3), 7.46 (d, $^3J_{\rm H,H}$=7.5 Hz, 1H, Py-H3, or Lu-H3), 7.34 (m, 2H, Py-H5, Lu-H5), 5.76 (m, 1H, C1H or C2H), 5.55 (m, 2H, C*H*$_2$NH), 5.40 (m, 1H, C1H or C2H, CH$_2$NH), 4.91 (m, 3H, C6H, C4H, C*H*$_2$NH), 4.32 (m, 1H, C5H), 3.85 (m, 1H, C8H), 3.30 (s, 3H, Lu-CH$_3$), 3.23 (m, 1H, C3H), 3.09 (m, 1H, C8H), 2.53 (m, 1H, C7H), 2.28 (m, 1H, C3H), 1.95 ppm (m, 1H, C7H).

Decomposition of 4^{2+}: [**4**](PF$_6$)$_2$ was dissolved in acetone, and the color changed from grayish to yellow within several minutes. Complexes **14**$^{2+}$ (50%) and **15**$^{2+}$ (50%, 3:1 mixture of **15**$_{\rm A}^{2+}$ and **15**$_{\rm B}^{2+}$) were obtained.

14^{2+}: ^{1}H NMR (300 MHz, [D$_6$]acetone, 298 K): δ=9.48 (d, $^3J_{\rm H,H}$=5.5 Hz, 1H, Py-H6), 8.06 (dt, $^3J_{\rm H,H}$=7.9 Hz, $^4J_{\rm H,H}$=1.5 Hz, 1H, Py-H4), 7.94 (t, $^3J_{\rm H,H}$=7.9 Hz, 1H, MePy-H4), 7.77–7.51 (m, 4H, Py-H3, Py-H5, MePy-H3, MePy-H5), m (5.84–5.11, 2H, C*H*$_2$NH), 5.32 (d, $^2J_{\rm H,H}$=19.0 Hz, 1H, Py-C*H*$_2$NH), 5.27–5.11 (m, 3H, MePy-C*H*$_2$NH, CH=CH), 4,83 (m, 2H, CH=CH), 3.3 (s, 3H, PyC*H*$_3$), 3.17–2.75 (m, 2H, CH=CH-C*H*$_2$-*exo*), 2.40–2.15 (m, 2H, CH=CHC*H*$_2$-*endo*), −9.78 ppm (s, 1H, IrH); ^{13}C NMR (75 MHz, [D$_6$]acetone, 298 K): δ=153.2 (Lu-C2), 152.7 (Py-C2), 152.0 (Lu-C6), 145.6 (Py-C6), 132.4 (Lu-C3), 132.3 (Py-C3), 118.8 (Py-C2), 118.6 (Py-C5), 115.5 (Lu-C5), 113.4 (Lu-C2), 80.1 (C=C), 79.6 (C=C), 71.5 (C=C), 69.0 (C=C), 56.1 (Lu-*C*H$_2$NH), 54.5 (Py-*C*H$_2$NH), 25.3 (C=C*C*H$_2$), 23.8 (Lu-Me), 22.1 (C=C*C*H$_2$), 20.6 (C=C*C*H$_2$), 19.7 (C=C*C*H$_2$). ESI$^+$-MS (acetone): *m/z*: 257.5 [**14**]$^{2+}$, 286.5 [**14**+acetone]$^{2+}$.

15$_{\rm A}^{2+}$: ^{1}H NMR (300 MHz, [D$_6$]acetone, 298 K): δ=8.61 (d, $^3J_{\rm H,H}$=5.7 Hz, 1H, Py-H6), 7.93 (t, $^3J_{\rm H,H}$=7.4 Hz, 1H, Py-H4), 7.82 (t, $^3J_{\rm H,H}$=7.8 Hz, 1H, Lu-H4), 7.66 (d, $^3J_{\rm H,H}$=8.1 Hz, 1H, Py-H3 or Lu-H3), 7.55–7.38 (m, 3H, Py-H3 or Lu-H3, Py-H5, Lu-H5), 5.40 (dd, $^3J_{\rm H,H}$=7.7 Hz, $^2J_{\rm H,H}$=18.8 Hz, 2H, C*H*$_2$NH), 5.26 (m, 2H, C1H, C2H), 5.09 (d, $^2J_{\rm H,H}$=16.5 Hz, 2H, C*H*$_2$NH), 4.88 (m, 1H, C6H or C4H), 4.52 (m, 1H, C6H or C4H), 4.35 (m 1H, C5H), 3.97 (m, 1H, C8H), 3.46 (m, 1H, C3H), 3.35 (s, 3H, Lu-CH$_3$), 2.95 (m, 1H, C8H), 2.55 (m, 2H, C7H, C3H), 1.67 (m, 1H, C7*H*). ESI$^+$-MS (acetone): *m/z*: 256.5 [**15**]$^{2+}$, 285.5 [**15**+acetone]$^{2+}$.

Decomposition of 5^{2+}: Complex **5**$^{2+}$ was formed in situ by addition of [D$_6$]acetone to a mixture of [**5**]PF$_6$ and AgPF$_6$. The mixture was stirred for several hours yielding [**7H**](PF$_6$)$_2$ and [**16**](PF$_6$)$_2$ in 1:1 ratio.

16^{2+}: ^{1}H NMR (300 MHz, [D$_6$]acetone, 298 K): δ=8.6–7.1 (m, 11H, PyH and PhH), 6.09 (d, $^2J_{\rm H,H}$=16.2 Hz, 1H, CH$_2$N), 5.97 (m, 1H, C1H or C2H), 5.83 (d, $^2J_{\rm H,H}$=12.9 Hz, 1H, CH$_2$N), 5.73 (m, 1H, C1H or C2H), 5.47 (d, $^2J_{\rm H,H}$=12.6 Hz, 1H, CH$_2$N), 5.19 (m, 1H, C6H), 4.95 (m, 2H, CH$_2$N, C4H), 4.79 (d, $^2J_{\rm H,H}$=16.5 Hz, 1H, CH$_2$N), 4.70 (d, $^2J_{\rm H,H}$=15.9 Hz, 1H, CH$_2$N), 4.67 (m, 1H, C5H), (4.61 (d, $^2J_{\rm H,H}$=8.4 Hz, 1H, CH$_2$N), 3.82 (d, 1H, C8H), 3.20–2.90 (m, 3H, C3H, C8H, C7H), 2.5 (m, 1H, C3H), 1.94 (m, 1H, C7*H*).

Decomposition of 6^{2+}: Complex **6**$^{2+}$ was generated in situ by addition of an excess of AgPF$_6$ to a solution of [**6**]PF$_6$ in acetone. The color changed to dark red-purple. The mixture was stirred for several minutes until a yellow reaction mixture was obtained. The solution was filtered and evaporated to yield cyclooctadienyl species **18**$^{2+}$ as the major product.

^{1}H NMR (300 MHz, [D$_6$]acetone, 298 K): δ=8.2–7.4 (m, 11H, PyH and PhH), 6.02 (d, $^2J_{\rm H,H}$=15.6 Hz, 1H, CH$_2$N), 5.79 (d, $^2J_{\rm H,H}$=12.6 Hz, 1H, CH$_2$N), 5.57 (d, $^2J_{\rm H,H}$=12.6 Hz, 1H, CH$_2$N), 5.5 (m, 1H, C1H or C2H), 5.3 (m, 1H, C1H or C2H), 5.05 (d, $^2J_{\rm H,H}$=17.0 Hz, 1H, CH$_2$N), 4.97 (d, $^2J_{\rm H,H}$=15.9 Hz, 1H, CH$_2$N), 4.9 (m, 1H, C6*H*), 4.7 (m, 2H, C*H*$_2$N, C4*H*), 3.9 (m, 1H, C5*H*), 3.83 (d, 1H, C8H), 3.2–2.9 (m, 3H, C3H, C8H, C7H), 2.2 (m, 1H, C3H), 1.7 ppm (m, 1H, C7H). (Traces of hydride species **17**$^{2+}$ were observed in the NMR spectrum: δ=−14.6 (IrH)). ^{13}C NMR (75 MHz, [D$_6$]acetone, 298 K): δ=162.7 (Py-C2), 161.5 (Py-C2 or Py-C6), 161.4 (Py-C2 or Py-C6), 158.1 (Py-C6), 140.5, 140.0 (PyC4), 132.8 (Ph-C1), 129.9 (Ph-C2), 129.3 (Ph-C3), 128.6 (Py-C4), 127.5, 127.3 (Py-C5), 122.1, 120.6 (Py-C3), 95.6 (C6), 93.5 (C4), 83.3 (C5), 70.2 (CH$_2$), 68.3 (CH$_2$), 62.0 (CH$_2$), 60.7 (C1), 59.3 (C2), 35.3 (Me), 27.9 (Me), 27.1 (C7), 24.0 (C3), 18.8 ppm (C8).

Synthesis of [(Me$_2$-tpa)Ir$^{\rm I}$(propene)]$^+$ (19$^+$): [{Ir$^{\rm I}$(μ-Cl)(coe)$_2$}$_2$] (500 mg, coe = cyclooctene) was suspended in methanol (40 mL) saturated with propene at room temperature. While bubbling propene through the methanol, Me$_2$-tpa (300 mg) was added to the suspension of [{(coe)$_2$Ir(μ-Cl)}$_2$]. To enhance the reaction, dichloromethane was added until a clear solution had been obtained. After 1 h of stirring and bubbling propene, NaBPh$_4$ (305 mg) was added to the solution. Evaporation of dichloromethane by bubbling propene through the solution caused precipitation of [Ir$^{\rm I}$(propene)(Me$_2$-tpa)]BPh$_4$. The orange-red precipitate was collected by filtration under a propene atmosphere and dried in vacuo. NMR spectroscopy indicated formation of two isomers in about 1:3 ratio (**19A**$^+$:**19B**$^+$). X-ray-quality crystals were obtained from a concentrated solution of [**19A**]BPh$_4$/[**19B**]BPh$_4$ in acetone to which a small amount of diethyl ether was added as nonsolvent, from which predominantly [**19B**]BPh$_4$ crystallized. Preparation of the PF$_6$ salt of **19**$^+$ was achieved via the same route, by using KPF$_6$ instead of NaBPh$_4$.

^{1}H NMR ([**19B**]BPh$_4$): 200 MHz, [D$_6$]acetone, 298 K): δ=8.59 (d, 1H, $^3J_{\rm H,H}$=5 Hz, Py-H6), 7.66 (several signals), 7.58 (d, 1H, $^3J_{\rm H,H}$=7.6 Hz, Py-H3), 7.33 (m, 8H, borate H2 and H6), 7.30–7.05 (several signals), 6.88 (t, 8H, $^3J_{\rm H,H}$=7.4 Hz, borate H3 and H5), 6.77 (t, 4H, $^3J_{\rm H,H}$=7.1 Hz, borate H4), 5.54 (d[AB], 1H, $^2J_{\rm H,H}$=14.3 Hz, NCH$_2$=Py$_{\rm Me}$), 5.16 (d[AB], 1H, $^2J_{\rm H,H}$=14.3 Hz, NCH$_2$Py$_{\rm Me}$ and d[AB], 1H, $^2J_{\rm H,H}$=17.5 Hz, NCH$_2$Py$_{\rm Me}$), 4.95 (s, 2H, NCH$_2$Py), 4.60 (d[AB], 1H, $^2J_{\rm H,H}$=17.5 Hz, NCH$_2$Py$_{\rm Me}$), 3.53 (s, 3H, Py$_{\rm Me}$-CH$_3$), 2.80 (s, 3H, Py$_{\rm Me}$-CH$_3$), 2.10 (dd, 1H, =CH$_2$, partially obscured by [D$_6$]acetone resonances), 1.89 (m, 1H,=CHCH$_3$), 1.29 (dd, 1H, $^3J_{\rm H,H}$=8.3 Hz, $^2J_{\rm H,H}$=3.8 Hz, =CH$_2$), 0.74 ppm (d. 3H, $^3J_{\rm H,H}$=6.4 Hz, =CH-CH$_3$).

^{1}H NMR ([**19A**]BPh$_4$): 200 MHz, [D$_6$]acetone, 298 K): δ=8.31 (d, 1H, $^3J_{\rm H,H}$=6.0 Hz, Py-H6), 7.60 (several signals), 7.56 (d, 1H, $^3J_{\rm H,H}$=7.6 Hz, Py-H3), 7.33 (m, 8H, borate H2 and H6), 7.30–7.05 (several signals), 6.88 (t, 8H, $^3J_{\rm H,H}$=7.4 Hz, borate H3 and H5), 6.77 (t, 4H, $^3J_{\rm H,H}$=7.1 Hz, borate H4), 5.41 (d[AB], 1H, $^2J_{\rm H,H}$=14.3 Hz, NCH$_2$), 5.25 (d[AB], 1H, $^2J_{\rm H,H}$=16.5 Hz, NCH$_2$), 5.05 (d[AB], 1H, $^2J_{\rm H,H}$=14.3 Hz, NCH$_2$), 4.95 (d[AB], 1H, $^2J_{\rm H,H}$=17.5 Hz, NCH$_2$), 4.89 (d[AB], 1H, $^2J_{\rm H,H}$=16.5 Hz, NCH$_2$), 4.61 (d[AB], 1H, $^2J_{\rm H,H}$=17.5 Hz, NCH$_2$), 3.48 (s, 3H, Py$_{\rm Me}$-CH$_3$), 2.90 (s, 3H, Py$_{\rm Me}$-CH$_3$), 1.78 (m, 1H, =CHCH$_3$), 1.64 (dd, 1H, $^3J_{\rm H,H}$=7.9 Hz, $^2J_{\rm H,H}$=4.1 Hz, =CH$_2$), 1.50 (dd, 1H, $^3J_{\rm H,H}$=7.9 Hz, $^2J_{\rm H,H}$=3.8 Hz, =CH$_2$), 0.48 ppm (d, 3H, $^2J_{\rm H,H}$=6.4 Hz, =CHCH$_3$). MALDI-TOF-MS: 553 [M]$^+$, 511 [M−propene]$^+$, 418 [M−propene−PyMe]$^+$, 404 [M−(propene)−CH$_2$−PyMe]$^+$. MALDI-TOF-MS peak match: M^+=551.193460, $M^+_{\rm calcd}$=509.192000 (Δ=−2.6 ppm) for the elemental composition C$_{23}$H$_{28}$N$_4$Ir. CV: $E_{\rm a}$=−165 mV, $E_{1/2}$=−200 mV, ΔE=69 mV.

Decomposition of in situ generated 19^{2+}: Dissolving [**19**]PF$_6$ and one equivalent of [Ag]PF$_6$ in acetonitrile results in formation of [**20**]$^{2+}$ and several hydride species. The hydride species and **20**$^{2+}$ have similar solubility properties, which prevents isolation of **20**$^{2+}$ as a pure compound. Complex **20**$^{2+}$ was identified by NMR spectroscopy of the mixture. The NMR interpretation of **20**$^{2+}$ is based on CH correlation, NOESY, and COSY experiments.

^{1}H NMR ([**20**](PF$_6$)$_2$, 500 MHz, [D$_3$]acetonitrile, 298 K): δ=8.28 (d, $^3J_{\rm H,H}$=5.9 Hz, 1H, Py-H6), 7.91 (t, $^3J_{\rm H,H}$=7.7 Hz, 1H, Py-H4), 7.82 (t, $^3J_{\rm H,H}$=7.7 Hz, 1H, Py-H4), 7.75 (t, $^3J_{\rm H,H}$=7.7 Hz, 1H, Py-H4), 7.61 (d, $^3J_{\rm H,H}$=8.0 Hz, 1H, Py-H3), 7.47 (d, $^3J_{\rm H,H}$=7.8, 1H, Py-H3), 7.31 (several signals, 3H, Py-H5), 7.23 (d, $^3J_{\rm H,H}$=6.5 Hz, 1H, Py-H3), 5.55 (d[AB], $^2J_{\rm H,H}$=16.1 Hz, 1H, NCH$_2$), 5.45 (d[AB], $^2J_{\rm H,H}$=15.6 Hz, 1H, NCH$_2$), 5.38 (d[AB] $^2J_{\rm H,H}$=16.1 Hz, 1H, NCH$_2$), 5.30 (d[AB] $^2J_{\rm H,H}$=15.7 Hz, 1H, NCH$_2$), 5.3 (m, 1H, propenyl-C$_2$CH), 5.16 (d[AB], $^2J_{\rm H,H}$=18.4 Hz, 1H, NCH$_2$), 4.99 (d, $^3J_{\rm H,H}$=6.9 Hz, 1H, propenyl-CH$_2$), 4.85 (d[AB], $^2J_{\rm H,H}$=18.4 Hz, 1H, NCH$_2$), 4.07 (d, $^3J_{\rm H,H}$=7.0 Hz, 1H, propenyl-CH$_2$), 3.35 (s, 3H, Py$_{\rm Me}$-CH$_3$), 3.15 (d, $^3J_{\rm H,H}$=11.4 Hz, 1H, propenyl-CH$_2$), 2.98 (d, $^3J_{\rm H,H}$=11.7 Hz, 1H, propenyl-CH$_2$), 2.53 ppm (s, 3H, Py$_{\rm Me}$-CH$_3$).

^{13}C NMR ([**20**](PF$_6$)$_2$, 125 MHz, [D$_3$]acetonitrile, 298 K): δ=164 (Py-C2s), 158 (Py-C6s), 152.2 (Py-C6), 140.5 (Py-C4), 139.9 (Py-C4), 139.4 (Py-C4), 135.6 (Py-C5), 135.6 (Py-C5), 126.9 (Py-C5), 126.7 (Py-C3), 126.2 (Py-C3), 119.8 (Py-C3), 102.4 (propenyl-CH), 73.8 (NCH$_2$), 71.6 (NCH$_2$), 68.8 (NCH$_2$), 44.1 (propenyl-CH$_2$), 38.0 (propenyl-CH$_2$), 30.0 (Py$_{\rm Me}$-CH$_3$), 25.1 ppm (Py$_{\rm Me}$-CH$_3$).

CCDC-218656–CCDC-218657 and CCDC-608078–CCDC-608083 contain the supplementary crystallographic data for this paper. These data can be obtained free of charge from the Cambridge Crystallographic Data Centre via www.ccdc.cam.ac.uk/data_request/cif. The crystallographic data of [**19**]BPh_4 were of poor quality. These data can be found in the Supporting Information and were not deposited at the CCDC.

Acknowledgements

This work was supported by the Netherlands Organization for Scientific Research (NWO-CW), the Radboud University of Nijmegen, and the University of Amsterdam. We thank Dr. Peter H. M. Budzelaar for helpful tips and tricks concerning the DFT calculations.

---

[1] a) F. M. Dixon, J. R. Farrell, P. E. Doan, A. Williamson, D. A. Weinberger, C. A. Mirkin, C. Stern, C. D. Incarviton, L. M. Liable-Sands, L. N. Zakharov, A. L. Rheingold, *Organometallics* **2002**, *21*, 3091–3093; b) D. G. DeWit, *Coord. Chem. Rev.* **1996**, *147*, 209–246; c) K. K. Pandey, *Coord. Chem. Rev.* **1992**, *121*, 1–42; d) A. M. Bond, D. G. Humphrey, D. Menglet, G. G. Lazarev, R. S. Dickson, T. Vu, *Inorg. Chim. Acta* **2000**, *300*, 565–571; e) N. G. Connelly, D. J. H. Emslie, W. E. Geiger, O. D. Hayward, E. B. Linehan, A. G. Orpen, M. J. Quayle, P. H. Rieger, *J. Chem. Soc. Dalton Trans.* **2001**, 670–683.

[2] a) X.-X. Zhang, B. B. Wayland, *J. Am. Chem. Soc.* **1994**, *116*, 7897–7898; b) X.-X. Zhang, G. F. Parks, B. B. Wayland, *J. Am. Chem. Soc.* **1997**, *119*, 7938–7944; c) W. H. Cui, X. P. Zhang, B. B. Wayland, *J. Am. Chem. Soc.* **2003**, *125*, 4994–4995.

[3] a) H Ogoshi, J. Setsunu, Z. Yoshida, *J. Am. Chem. Soc.* **1976**, *98*, 3869–3870; b) B. B. Wayland, Y. Feng, S. Ba, *Organometallics* **1989**, *8*, 1438–1441; c) B. B. Wayland, G. Poszmik, M. Fryd, *Organometallics* **1992**, *11*, 3534–3542.

[4] a) R. H. Crabtree, *The Organometallic Chemistry of the Transition Metals*, Wiley-Interscience, New York, **1994**; b) R. A. Van Santen, P. W. N. M. Van Leeuwen, J. A. Moulijn, B. A. Averill, *Catalysis: An Integrated Approach*, Elsevier, Amsterdam, **1999**.

[5] D. G. H. Hetterscheid, J. Kaiser, E. Reijerse, T. P. J. Peters, S. Thewissen, A. N. J. Blok, J. M. M. Smits, R. de Gelder, B. de Bruin, *J. Am. Chem. Soc.* **2005**, *127*, 1895–1905.

[6] D. G. H. Hetterscheid, M. Bens, B. de Bruin, *Dalton Trans.* **2005**, 979–984.

[7] In a previous communication we already reported this unusual behavior for $[(Rh^{II}(cod)(dpa)]^{2+}$: D. G. H. Hetterscheid, B. de Bruin, J. M. M. Smits, A. W. Gal, *Organometallics* **2003**, *22*, 3022–3024.

[8] A. D. Burrows, M. Green, J. C. Jeffery, J. M. Lynam, M. F. Mahon, *Angew. Chem.* **1999**, *111*, 3228–3230; *Angew. Chem. Int. Ed.* **1999**, *38*, 3043–3045; .

[9] B. De Bruin, J. A. Brands, J. J. J. M. Donners, M. P. J. Donners, R. de Gelder, J. M. M. Smits, A. W. Gal, A. L. Spek, *Chem. Eur. J.* **1999**, *5*, 2921–2936.

[10] A. R. Rossi, R. Hoffmann, *Inorg. Chem.* **1975**, *14*, 365–374.

[11] D. G. H. Hetterscheid, J. M. M. Smits, B. de Bruin, *Organometallics* **2004**, *23*, 4236–4246.

[12] B. A. Goodman, J. B. Raynor, *Electron Spin Resonance of Transition Metal Complexes in Advances in Inorganic Chemistry and Radiochemistry* (Eds.: H. J. Emeléus, A. G. Sharpe), **1970**, *13*, 136–362.

[13] N. G. Connely, D. J. H. Emslie, P. Klangsinsirikul, P. H. Rieger, *J. Phys. Chem. A* **2002**, *106*, 12214–12220.

[14] For (nearly) axial *A* tensors, the dipolar part *T* of the hyperfine tensor is calculated from $T=(A_{avg}-A_{\perp})$ with $A_{avg}=(A1+A2+A3)/2$ (and in this case $A_{-=}(A1+A2)/2$ from the slightly rhombic tensor). The spin density at N3 in the 2s orbital sd_{2s} is calculated from $sd_{2s}=A_{avg}/1443.9$, and for the 2p orbital $sd_{2p}=T/49.8$ (1443.9 MHz and 49.8 MHz are hyperfine couplings for a nitrogen atom with 100 % spin density in a 2s and 2p orbital, respectively). See also reference [16].

[15] B. B. Wayland, A. E. Sherry, A. G. Bunn, *J. Am. Chem. Soc.* **1993**, *115*, 7675–7684.

[16] T. Büttner, J. Geier, G. Frison, J. Harmer, C. Calle, A. Schweiger, H. Schönberg, H. Grützmacher, *Science* **2005**, *307*, 235–238.

[17] D. G. H. Hetterscheid, B. de Bruin, *J. Mol. Catal. A* **2006**, *251*, 291–296.

[18] Further shielding of the metal center by a second PyMe group by using the ligand *N*,*N*-bis(6-methyl-2-pyridylmethyl)amine (dla) leads to M^{II} species $[M^{II}(cod)(dla)]^{2+}$ with increased stability compared to $[M^{II}(cod)(pla)]^{2+}$. We did not further investigate these complexes.

[19] a) M. P. García, M. V. Jiménez, L. A. Oro, F. J. Lahoz, P. J. Alonso, *Angew. Chem.* **1992**, *104*, 1512–1514; *Angew. Chem. Int. Ed. Engl.* **1992**, *31*, 1527–1529; b) M. P. García, M. V. Jiménez, L. A. Oro, F. J. Lahoz, J. M. Casas, P. J. Alonso, *Organometallics*, **1993**, *12*, 3257–3263.

[20] a) M. J. Shaw, W. E. Geiger, J. Hyde, C. White, *Organometallics* **1998**, *17*, 5486; b) M. J. Shaw, J. Hyde, C. White, W. E. Geiger, *Organometallics* **2004**, *23*, 2205–2208.

[21] a) J. F. Kohnle, L. H. Slaught, K. L. Nakamaye, *J. Am. Chem. Soc.* **1969**, *91:21*, 5904–5905; b) R. G. Salomon, N. El Sanadi, *J. Am. Chem. Soc.* **1975**, *97:21*, 6214–6221.

[22] At higher $[H^+]$ and [MeCN] the relative influence of impurities on the k_{obs} values obviously becomes less important. To diminish the effect caused by impurities on the relative k^H_{obs} and k^D_{obs} values required for KIE measurements, at least about 0.4 equiv of H^+ and about 0.4 equiv of MeCN should be added. Unfortunately, under such conditions the reaction becomes too fast to follow with our experimental setup, and KIE measurements become unreliable.

[23] See, for example: a) X. Hu, I. Castro-Rodriguez, K. Meyer, *J. Am. Chem. Soc.* **2004**, *126*, 13464–13473; b) A. Nemes, A. Bakac, *Inorg. Chem.* **2001**, *40*, 2720–2724; c) K. Matyjaszewski; J. Xia, *Chem. Rev.* **2001**, *101*, 2921–2990.

[24] An electronic effect might also play a role: Dissociation of a pyridyl donor results in an unsaturated species. To compensate for the loss of the fifth donor, the remaining N donors will tend to bind more strongly. NH_{amine} and N_{Py} are then better suited to compensate for the electronic unsaturation compared to BnN_{amine} and N_{PyMe} donors.

[25] The energies associated with Py dissociation should actually be somewhat lower because we did not correct for the entropy contribution.

[26] W. L. F. Amarego, D. D. Perrin, *Purification of Laboratory Chemicals*, 4th Ed., Butterworth-Heinemann, Oxford, **1996**.

[27] a) G. Giordano, R. H. Crabtree, *Inorg. Synth.* **1990**, *28*, 88–90; b) G. Winkhaus, H. Singer, *Chem. Ber.* **1966**, *99*, 3610–3618; c) J. L. Herde, J. C. Lambert, C. V. Senoff, *Inorg. Synth.* **1974**, *15*, 18–20; d) H. Nagao, N. Komeda, M. Mukaida, M. Suzuki, K. Tanaka, *Inorg. Chem.* **1996**, *35*, 6809–6815.

[28] A. L. Spek, PLATON, A Multipurpose Crystallographic Tool, Utrecht University, Utrecht, The Netherlands, **2003**.

[29] P. T. Beurskens, G. Beurskens, W. P. Bosman, R. de Gelder, S. García-Granda, R. O. Gould, R. Israël, J. M. M. Smits, DIRDIF-96, A computer program system for crystal structure determination by Patterson methods and direct methods applied to difference structure factors, Laboratory of Crystallography, Department of Inorganic Chemistry, University of Nijmegen, The Netherlands, **1996**.

[30] P. T. Beurskens, G. Beurskens, M. Strumpel, C. E. Nordman in *Patterson and Pattersons* (Eds.: J. P. Glusker, B. K. Patterson, M. Rossi) Clarendon Press, Oxford, **1987**,p. 356.

[31] G. M. Sheldrick, SHELXL-97, Program for the refinement of crystal structures, University of Göttingen, Germany, **1997**.

[32] a) Turbomole Version 5, R. Ahlrichs, M. Bär, H.-P. Baron, R. Bauernschmitt, S. Böcker, M. Ehrig, K. Eichkorn, S. Elliott, F. Furche, F. Haase, M. Häser, C. Hättig, H. Horn, C. Huber, U. Huniar, M. Kattannek, A. Köhn, C. Kölmel, M. Kollwitz, K. May, C. Ochsenfeld, H. Öhm, A. Schäfer, U. Schneider, O. Treutler, K. Tsereteli, B. Unterreiner, M. von Arnim, F. Weigend, P. Weis, H. Weiss, Theoretical Chemistry Group, University of Karlsruhe, Jan. **2002**; b) O. Treutler, R. Ahlrichs, *J. Chem. Phys.* **1995**, *102*, 346–354; c) Turbomole basisset library, Turbomole Version 5;[32a] d) A. Schä-

fer, H. Horn, R. Ahlrichs, *J. Chem. Phys.* **1992**, *97*, 2571–2577; e) D. Andrae, U. Haeussermann, M. Dolg, H. Stoll, H. Preuss, *Theor. Chim. Acta* **1990**, *77*, 123–141; f) A. Schäfer, C. Huber, R. Ahlrichs, *J. Chem. Phys.* **1994**, *100*, 5829–5835.

[33] a) PQS version 2.4, **2001**, Parallel Quantum Solutions, Fayetteville, Arkansas, USA (the Baker optimizer is available separately from PQS upon request); b) J. Baker, *J. Comput. Chem.* **1986**, *7*, 385–395.

[34] a) A. D. Becke, *Phys. Rev. A* **1988**, *38*, 3098–3100; b) J. P. Perdew, *Phys. Rev. B* **1986**, *33*, 8822–8824.

[35] a) C. Lee, W. Yang, R. G. Parr, *Phys. Rev. B* **1988**, *37*, 785–789; b) A. D. Becke, *J. Chem. Phys.* **1993**, *98*, 1372–1377; c) A. D. Becke *J. Chem. Phys.* **1993**, *98*, 5648–5652, d) All calculations were performed with the Turbomole functional "b3-lyp", which is not identical to the Gaussian "B3LYP" functional.

[36] Lead reference for calculation of *g* tensor (Zeeman interactions) parameters: E. van Lenthe, A. van der Avoird, P. E. S Wormer, *J. Chem. Phys.* **1997**, *107*, 2488–2498. Lead reference for calculation of *A* tensor (nuclear magnetic dipole hyperfine interactions) parameters: E. van Lenthe, A. van der Avoird, P. E. S. Wormer, *J. Chem. Phys.* **1998**, *108*, 4783–4796.

[37] ADF2004.01, a) E. J. Baerends, D. E. Ellis, P. Ros, *Chem. Phys.* **1973**, *2*, 41–51; b) L. Versluis, T. Ziegler, *J. Chem. Phys.* **1988**, *88*, 322–328; c) G. te Velde, E. J. Baerends, *J. Comput. Phys.* **1992**, *99(1)*, 84–98; d) C. Fonseca Guerra, J. G. Snijders, G. te Velde, E. J. Baerends, *Theor. Chem. Acc.* **1998**, *99*, 391–403.

Received: May 22, 2006
Revised: September 28, 2006